THE ASTROPHYSICAL JOURNAL, 396:62–79, 1992 September 1

THE COMPACT TRIPLES 0710+439 AND 2352+495: A NEW MORPHOLOGY OF RADIO GALAXY NUCLEI

J. E. CONWAY,[1] T. J. PEARSON, A. C. S. READHEAD, S. C. UNWIN, AND W. XU
Owens Valley Radio Observatory, Mail Code 105-24, California Institute of Technology, Pasadena, CA 91125

AND

R. L. MUTEL
Department of Physics and Astronomy, University of Iowa, Iowa City, IA 52242
Received 1991 December 10; accepted 1992 March 9

ABSTRACT

The compact radio sources 0710+439 and 2352+495 have each been mapped using intercontinental VLBI arrays at frequencies of 5.0 and 10.7 GHz. The source 0710+439 has also been mapped at 1.7 GHz. Both sources consist of three principal components that lie almost on a straight line. Except for the existence of three VLBI components instead of two they both seem to have similar properties to members of the compact double class. Multi-epoch observations show that apparent velocities between the components in both sources are below *c*. In the source 0710+439 comparison of multi-epoch data allows us to set a limit of 0.054 ± 0.14 h^{-1} *c* on the rate of separation of the two brightest components. In 2352+495 the multi-epoch 5 GHz VLBI data show that the flux density variations detected by total flux density monitoring are due to changes within the middle component. These fluctuations may be due to refractive interstellar scintillation or they may be intrinsic to the source; in either case the middle component must contain the most compact structure within the source. The morphology, spectra and variability of the middle components strongly suggest that the center of activity in both sources lies here rather than in either of the outer components, providing the first clear evidence of *symmetric* radio structure in a powerful active galaxy nucleus.

Subject headings: galaxies: active — galaxies: individual (0710+439, 2352+495) — galaxies: nuclei — radio continuum: galaxies — techniques: interferometric

1. INTRODUCTION

We are engaged in a VLBI survey at 5 GHz of the structure of bright radio sources north of declination 35° (Pearson & Readhead 1988). Many of the sources are barely resolved on transatlantic baselines; but among those with structure on scales $\gtrsim 2$ mas, most are linear with a flat-spectrum "core" at one end of a steeper-spectrum "jet," and a few consist of two well-separated components (Pearson & Readhead 1988). One source in our sample, 0710+439, was unusual in that it consisted of three colinear components (see Fig. 1*a*). In order to more fully investigate this source we made additional observations of this source at 1.6 and 10.7 GHz. Analysis of third epoch 5 GHz observations of another survey source, 2352+495, and re-analysis of earlier 5 GHz observations have shown that this source has a structure very similar to that of 0710+439 (Fig. 1*b*).

Both 0710+439 and 2352+495 have radio spectra that peak in the gigahertz range and are therefore members of the class of radio source known as "Gigahertz Peaked Spectrum" (or GPS) sources (O'Dea, Baum, & Stanghellini 1991). A subclass of these GPS sources known as "Compact Doubles" (Mutel, Hodges, & Phillips 1985) show two equally bright VLBI scale components. The sources 0710+439 and 2352+495 share virtually all the radio and optical properties with these compact doubles, however, their triple structures make them distinct. We believe, based on the strikingly similar structures of these two sources that there is some fundamental physical process which produces this new type of "compact triple" source. In this paper we consider the origin of the triple structure and briefly consider the relationship between these sources and the compact doubles.

2. PREVIOUS OBSERVATIONS

2.1. *Optical Properties*

The radio source 0710+439 is identified with a 20 mag galaxy. Peacock et al. (1981) obtained a deep CCD image which showed that this object is extended with an *r* magnitude of 19.7 ± 0.2. The emission-line redshift of the galaxy is $z = 0.518 \pm 0.001$ (Lawrence et al. 1986). At this redshift, 1 mas = 3.5 h^{-1} pc assuming $H_0 = 100\ h$ km s^{-1} Mpc^{-1} and $q_0 = 0.5$. Optical spectra (C. R. Lawrence 1992, private communication) show prominent narrow O II and O III lines and some Hβ. The spectrum shows absorption lines characteristic of evolved stellar populations and the continuum shape is well fitted by that of an elliptical galaxy with no evidence for any nonstellar continuum.

Peacock & Wall (1981) identified 2352+495 as a galaxy and estimated a *V*-magnitude of 20.1, again from the Palomar Sky Survey. The emission-line redshift of the galaxy is $z = 0.237 \pm 0.001$ (Burbidge & Crowne 1979). At this redshift, 1 mas = 2.35 h^{-1} pc. Optical spectra (C. R. Lawrence 1992, private communication) show prominent O II and O III lines and some Hβ. The optical continuum shows no significant nonthermal contribution; the continuum shape and the presence of stellar absorption lines indicate that the galaxy is an elliptical. Recent CCD images by O'Dea, Baum, & Morris (1990) show distortions in the elliptical isophotes of this galaxy and the presence of some nearby sources.

---

[1] Postal address: National Astronomy Observatory, Socorro, NM 87801.

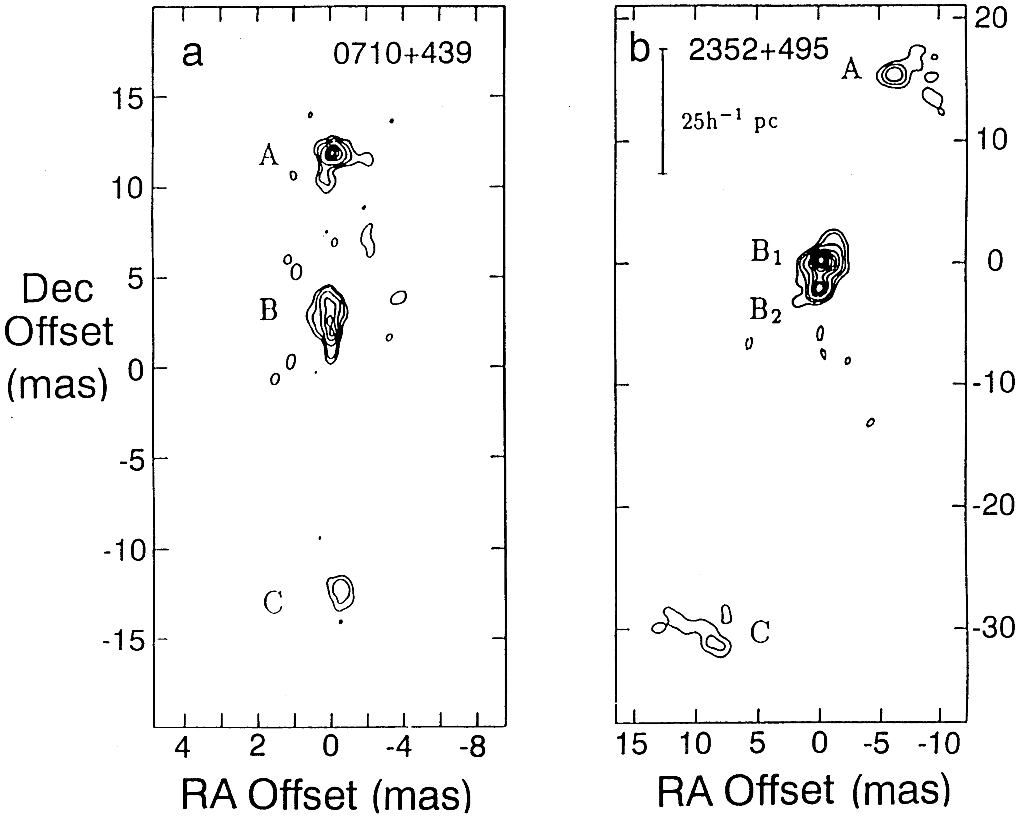

FIG. 1.—Maps of 0710+439 and 2352+495 on the same linear scale and approximately the same linear resolution. (*a*) A 10.7 GHz map of 0710+439. Restoring beam is 0.8 by 0.5 mas position angle −20°. Peak flux density is 133.7 mJy beam^{-1}, contour levels are at −5%, 5%, 10%, 20%, 30%, 40%, 50%, 60%, 70%, 80%, and 90% of the peak. (*b*) A 4.99 GHz map of 2352+495. Restoring beam is 1 mas circular. Peak is 34.8 mJy beam^{-1}, contour levels at −5%, −2%, 2%, 5%, 10%, 20%, 30%, 40%, 50%, 60%, 70%, 80%, and 90% of peak.

2.2. *Radio Structure*

The source 0710+439 has been mapped at 5 GHz and 1.4 GHz at the VLA, where it is used as a phase calibrator (Perley 1982, and private communication). At neither frequency is more than 0.2% of the flux density emitted on a scale of more than 1″. Rudnick & Jones (1983) detected no significant polarization at 4.9 and 15.0 GHz, with (3 σ) upper limits of 0.3% and 0.6%, respectively.

The results of first-epoch 5 GHz VLBI observations were published by Pearson & Readhead (1988). These observations showed the overall triple structure of the source and its unusual morphology. Despite having three components this source was provisionally classified as a compact double based on the fact that more than 80% of the emission came from two almost equally bright components. Comparison of first- and second-epoch 5 GHz observations separated by 2.5 yr showed no evidence for component movement (Readhead, Pearson, & Unwin 1984). In addition, comparison of the 5 GHz map with a map at 10.7 GHz suggested that the flattest spectrum part of this source was located toward the southern end of the middle component.

The source 2352+495 has been observed using the VLA and shows no radio emission on scales greater than 0″.2 (Perley 1982) at a level of greater than 0.4% of the total flux density. WSRT observations at 608 MHz (Baum et al. 1990) limit extended emission to less than 0.2% of total flux density on scales greater than 30″. VLA observations (Rudnick & Jones 1983) give fractional polarizations of 0.5% at 15 GHz and 0.7% at 5 GHz and a limit of ≤0.5% at 1.4 GHz.

A first epoch 5 GHz VLBI map of 2352+495 was presented by Pearson & Readhead (1988). This map showed only two main regions of emission. The authors noted that the maps and model fits provided only a rather poor fit to the visibility data and that a significant amount of emission was present on scales larger than 10 mas. However, based on the two almost equally bright components this source was provisionally classified as a compact double. Subsequent analysis of first, second and third epoch 5 GHz data (see § 4.2) revealed a previously undetected component to the south giving 2352+495, an overall morphology strikingly similar to 0710+439. This compact triple morphology was first noted in preliminary reports by Conway et al. (1990b, c).

2.3. *Radio Spectrum*

Total flux density measurements of 0710+439 and 2352+495 have been made at a number of frequencies (see Figs. 2 and 3). In view of the long-term variability of 0710+439 (see § 2.4), caution should be used in interpreting the spectrum of this source, which is made up of observations spread over about 15 yr. It is clear, however, that this is a typical "centimeter-excess" spectrum, with a peak around 3 GHz. There is no evidence for a steep-spectrum low-frequency component. The simple form of the spectrum could be interpreted as arising from a single, probably inhomogeneous,

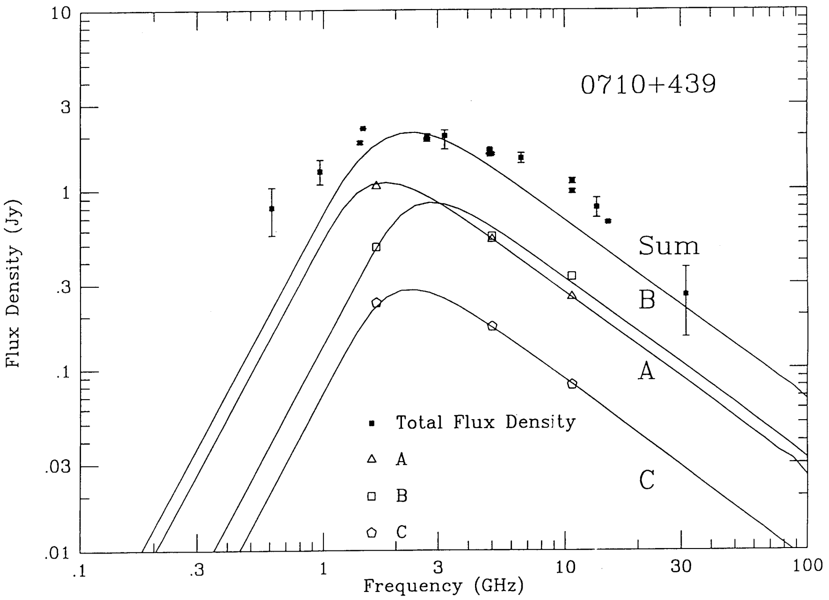

FIG. 2.—Radio spectrum of 0710+439. Total flux density measurements are from the following references (with observing frequency given first): 611 MHz, MacLeod et al. (1965); 966, Cohen et al. (1977); 1410, Witzel et al. (1979); 1464, Perley (1982); 2695, Kuhr et al. (1981); 2700, Bridle et al. (1977); 3200, Wills et al. (1971); 4885, Perley (1982); 4885, Rudnick & Jones (1983); 4900, Pauliny-Toth et al. (1978); 4995, Kapahi (1981); 6600, Wills et al. (1971); 10695, Kuhr et al. (1981), 10695, Seielstad et al. (1983); 13500, Wills et al. (1971); 15035, Rudnick & Jones (1983); 31400, Witzel et al. (1978).

The flux densities of the three VLBI components (A, B, C) are indicated. The solid curves marked A, B, and C show the theoretical spectra of three homogeneous synchrotron-radiating sources adjusted to fit the measurements of each component, and the curve marked "Sum" is the sum of these three model spectra.

synchrotron-radiating component; but the VLBI maps show that this interpretation is incorrect. The spectral radio luminosity of the source at the peak of the spectrum (2.8 GHz, corresponding to 4.5 GHz in the frame of the galaxy) is $2.2 \times 10^{34}\ h^{-2}$ ergs s^{-1} Hz^{-1}. The corresponding bolometric radio luminosity obtained by integrating the spectrum up to 100 GHz is about $2 \times 10^{44}\ h^{-2}$ ergs s^{-1}.

The spectrum of 2352+495 is similar to that of 0710+439 except that it is somewhat flatter with a peak which occurs at a lower frequency (around 1 GHz) (see Fig. 2). Variability in this source seems to be modest and confined to time scales much less than 1 yr (see next section) and so the combination of flux density measurements over 20 yr should not seriously distort the spectrum. The radio luminosity of the source at the peak of

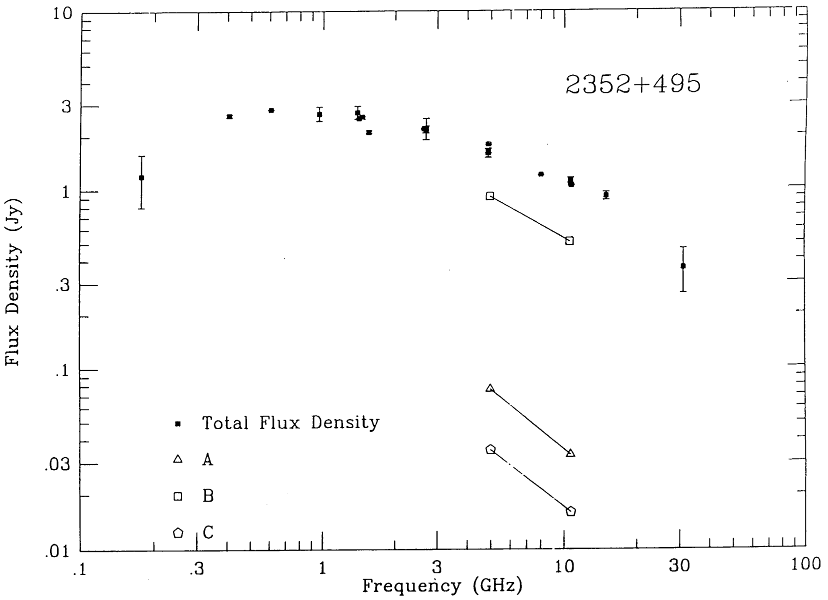

FIG. 3.—Radio spectrum of 2352+495. Total flux density measurements are from the following references (with observing frequency given first): 178 MHz, Fanaroff & Blake (1972); 408, Gregoroni et al. (1984); 608, Baum et al. (1990), 966, Cohen et al. (1977); 1400, Witzel et al. (1971); 1420, 1465, Perley (1982); 1565, Rudnick & Jones (1982); 2650, Kuhr et al. (1981); 2695, Kuhr et al. (1981); 2695, Fiedler et al. (1987); 2700, Peacock & Wall (1981); 4885, Perley (1982); 4885, Rudnick & Jones (1982); 4900, Pauliny-Toth et al. (1978); 8085, Fiedler et al. (1987); 10695, Kellerman & Pauliny-Toth (1973); 10800, Seilstad et al. (1983); 15035, Rudnick & Jones (1982); 31400, Witzel et al. (1978).

The flux densities of the three VLBI components (A, B, C) are also indicated.

the spectrum (1 GHz, corresponding to 1.24 GHz in the frame of the galaxy) is $3 \times 10^{33}\ h^{-2}$ ergs s^{-1} Hz^{-1}. The bolometric radio luminosity of 2352+495 up to 100 GHz is approximately $3 \times 10^{43}\ h^{-2}$ ergs s^{-1}.

2.4. *Radio Variability*

The total flux density of 0710+439 is known to vary at several radio frequencies. Variations were first reported at 1.6 GHz (Webber, DeNoyer, & Yang 1975), and the source was monitored at this wavelength from 1973 to 1979 at the Vermilion River Observatory (Webber et al. 1976; Webber, Yang, & Swenson 1980). During this period the flux density ranged from 1.7 to 2.2 Jy. There is some evidence for variability at 966 MHz also: Cohen et al. (1977) detected a ~20% increase in flux density at 966 MHz between their original survey of 1972–1973 and their later interferometer observations of 1973–1974. The 10.7 GHz flux density was monitored from 1979 to 1983 at the Owens Valley Radio Observatory (Seielstad, Pearson, & Readhead 1983); 13 measurements made between 1979.0 and 1983.0 are consistent with a constant flux density of 0.980 ± 0.013 Jy; any variation during this period was less than 0.1 Jy.

Total flux density monitoring of 2352+495 shows modest but definite variations on time scales of months at 2695 and 8085 MHz (Waltman et al. 1991), and at 10.7 GHz (Seielstad et al. 1983). The observations at 2695 MHz show peak to peak variations of 10%–15% during the period 1983–1986. Comparison of observations at 1.4 and 5 GHz separated by 10–15 yr shows no longer term component to the flux density variability.

3. VLBI OBSERVATIONS OF 0710+439

3.1. *Observations*

We have made maps of the milliarcsecond structure of 0710+439 at frequencies of 1.66, 5, and 10.7 GHz using telescopes of the US VLBI Network, the European VLBI network (EVN) and the 26 m telescope of the Dominion Radio Astrophysical Observatory. At 5 GHz there are observations at three epochs spread over 7 yr. The details of the VLBI observations are presented in Table 1. The maximum resolution obtained was approximately 3 mas at 1.66 GHz, 1 mas at 5.01 GHz, and 0.5 mas at 10.7 GHz.

All observations were made in left circular polarization (IEEE convention) and a bandwidth of 1.8 MHz was recorded using the Mark-II format (Clark 1973). The data were cross-correlated with the JPL-Caltech VLBI Processor. After preliminary calibration in the usual way (Cohen et al. 1975), maps were made using the self-calibration algorithms of Readhead & Wilkinson (1978) and Cornwell & Wilkinson (1981), as implemented in the Caltech VLBI package (Pearson 1991).

3.2. *General Morphology*

Maps of 0710+439 at each of the frequencies 1.6, 5, and 10.7 GHz are shown in Figure 4. In addition Figure 1*a* shows a full resolution map at 10.7 GHz and Figure 5 shows the three epochs at 5 GHz. The quality of the maps is limited by the accuracy of the calibration and UV-coverage. The estimated dynamic range, defined as the ratio of peak to the weakest feature which we believe is real varies from about 20:1 at 10.7 GHz to 100:1 at 5 GHz. All the maps clearly show the triple structure of the source. The three components will be referred to as A, B, and C, in order from north to south, as shown in Figure 1*a*. The major components lie close to a straight line with position angle (p. a.) 0° and show overall curvature (projected on the plane of the sky) of only $\angle ABC = 3° \pm 1°$. The total angular size of 0710+439 is 24.1 mas, corresponding to a projected linear size of 83.8 h^{-1} pc.

Table 2 lists Gaussian model fits to the main components found at each of the three frequencies. The fits found at 5 GHz are for the third epoch data. At 5 GHz the middle component is fitted by two Gaussian subcomponents denoted B_1 and B_2. For the 10.7 GHz map it was not possible to fit a simple Gaussian model to the middle component and so no 10.7 GHz fit is presented in Table 2. The fitting was done with the AIPS program JMFIT, which attempts to deconvolve the restoring beam. We expect (based on imaging simulations; see Appendix, § A1) that the relative peak brightness and flux density of components within the 5 GHz and 1.6 GHz maps should be accurate at the 10%–15% level and that dimensions larger than half the restoring beam are accurate at the 20% level. Dimensions smaller than half the restoring beam, such as the east-west dimension of B at 5 GHz, are described as "unresolved" principally because of uncertainties in the amplitude calibration of the longest baselines.

The middle component B is resolved along the north-south axis of the source at all three frequencies, but is unresolved in the east-west direction (width ≤0.4 mas from model-fitting at 5 GHz and a similar limit from the 10.7 GHz map). The angular size of component A is 2.5 × 1.8 mas at 1.6 GHz, but it appears smaller at higher frequencies, with an angular size of

TABLE 1

JOURNAL OF OBSERVATIONS OF 0710+439

Parameter	1.66 GHz	5.01 GHz	4.99 GHz	4.99 GHz	10.65 GHz
Epoch	1982.76	1980.53	1982.93	1986.89	1982.10
Duration (hr)	12	11	12	4 × 1	12
Antennas[a]	BKGIYOHP	BKGFO	BKGFO	SJBWKGFYO	BKGFO
Maximum baseline ($M\lambda$)	45	136	136	136	289

[a] S—26 m, Onsala Space Observatory, Onsala, Sweden; J—25 m, MkII Telescope, Jodrell Bank, Cheshire, UK; B—100 m, Max-Planck-Institut für Radioastronomie, Effelsberg, Germany; W—14 × 25 m, Phased array, Westerbork Synthesis Radio Telescope, Netherlands; K—36.6 m, Haystack Observatory of the Northeast Radio Observatory Corporation, Westford, Massachusetts; G—42.7 m, National Radio Astronomy Observatory, Green Bank, West Virginia; I—18.3 m, North Liberty Radio Observatory of the University of Iowa, North Liberty, Iowa; F—26 m, George R. Agassiz Station of Harvard University, Fort Davis, Texas; Y—25 m, one antenna of the NRAO Very Large Array, Socorro, New Mexico; O—40 m, Owens Valley Radio Observatory of the California Institute of Technology, Big Pine, California; H—25.9 m, Hat Creek Observatory of the University of California, Cassel, California; P—25.6 m, Dominion Radio Astrophysical Observatory of the National Research Council of Canada, Penticton, British Columbia, Canada.

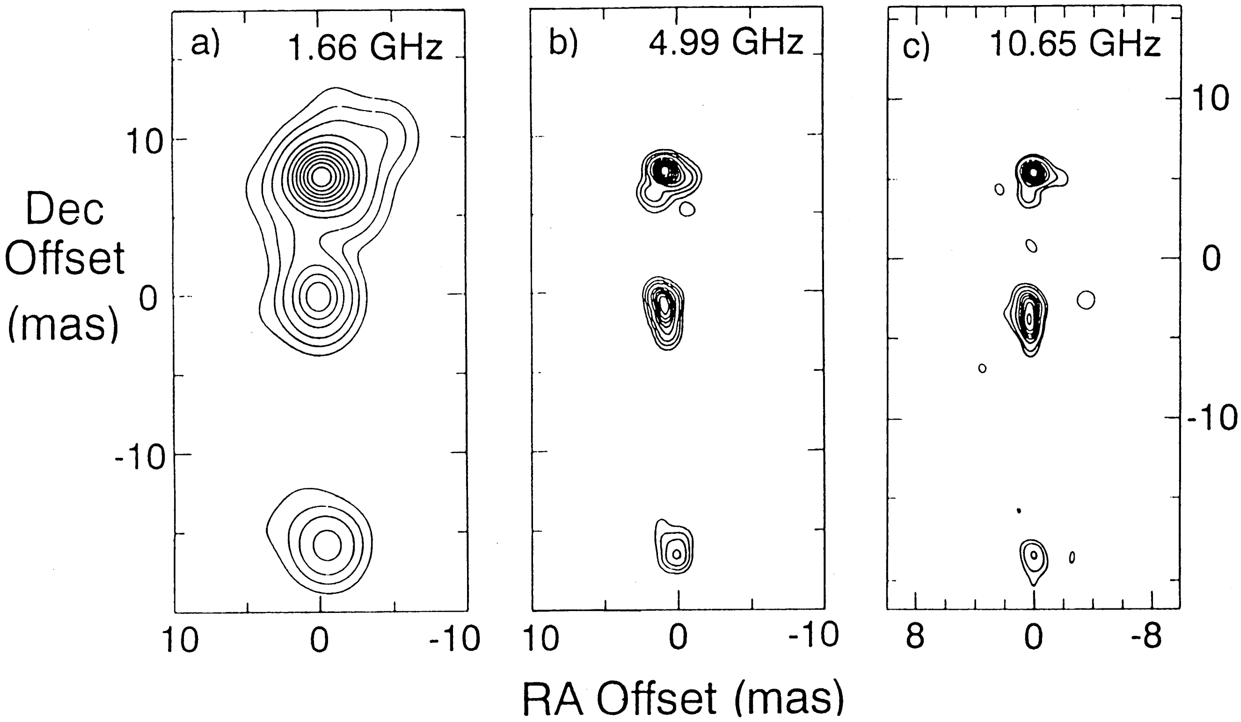

FIG. 4.—Hybrid maps of 0710+439 at 1.66, 4.99, and 10.7 GHz. (*a*) 1.66 GHz map, restoring beam 3 mas circular. Peak is 775.8 mJy beam^{-1}. The contour levels are −5%, −2%, 2%, 5%, 10%, 20%, 30%, 40%, 50%, 60%, 70%, 80%, and 90% of the peak brightness; negative contours are dashed. (*b*) 4.99 GHz map. The best 5 GHz map made from third epoch data (epoch 1986.89). Restoring beam is 1 mas circular. Peak is 322 mJy beam^{-1}. The contour levels are −5%, −2%, 2%, 5%, 10%, 20%, 30%, 40%, 50%, 60%, 70%, 80%, and 90% of the peak brightness; negative contours are dashed. (*c*) 10.7 GHz map, at epoch 1982.10. Restoring beam is 1 mas circular (see Fig. 1*a* for a higher resolution version). Peak is 187.4 mJy beam^{-1}. Contour levels are −5%, 5%, 10%, 20%, 30%, 40%, 50%, 60%, 70%, 80%, and 90% of the peak brightness; negative contours are dashed.

1.2 mas at 5 GHz. Component C is resolved in both dimensions, like A, with an angular size less than 1.35 mas. At 5 GHz component B accounts for about half the flux density of the source, while A and C account for 35% and 15%, respectively. At this frequency the ratio of the flux densities A:C is 3.4 and the ratio of the "arm lengths" AB:BC is 1.89.

3.3. *Comparison of Multi-Epoch Data*

To decide whether there is any evidence for any changes within this source we begin by comparing the closure phase data at different epochs as described in the Appendix, § A2. In general most closure triangles show no detectable change over the 6.33 yr between epochs 1 and 3. We note in particular the stability of the rapid 360° jump in closure phases at 1130 GST on the triangle BONN-NRAO-OVRO; the top panel of Figure 6 shows how the third epoch model fits the first epoch data. This feature is very sensitive to changes in the relative positions of the components and can be used to set sensitive limits on their relative velocities. The bottom panels of Figure 6 show the difference between the first epoch closure phases and model closure phases calculated from variants of the third-epoch model which contain different north-south shifts of the CLEAN components within component A. The reduced chi-squared fit (agreement factor) varies quadratically from a minimum of 1.5 at 0.03 mas to 2.3 for a shift of 0.1 mas, and 4.5 for a shift of 0.2 mas. For comparison a best fit to the third epoch data with agreement factor 1.047 is obtained for a shift of 0.05 mas of A. Taking the difference between the positions of

TABLE 2

GAUSSIAN FITTING OF 0710+439

Component	Frequency (GHz)	Flux Density (Jy)	Major (mas)	Minor (mas)	Position Angle	$B_{\rm me}$ (10^{-2} G)	$U_{\rm me}$ (10^{-4} ergs cm^{-3})
A	1.66	1.110	2.47	1.84	109°	3.3	1.0
	4.99	0.529	0.95	0.68	72	7.9	5.8
	10.65	0.253	0.76	0.42	80	10.0	9.3
B	1.66	0.480	2.19	1.03	9	3.5	1.1
B_1	4.99	0.359	1.86	0.39	−30	6.7	4.2
B_2	4.99	0.202	1.16	0.42	9	6.8	4.3
C	1.66	0.232	1.62	1.61	57	2.6	0.6
	4.99	0.172	1.35	1.05	29.3	4.0	1.5
	10.65	0.081	1.22	0.80	25	4.5	1.9

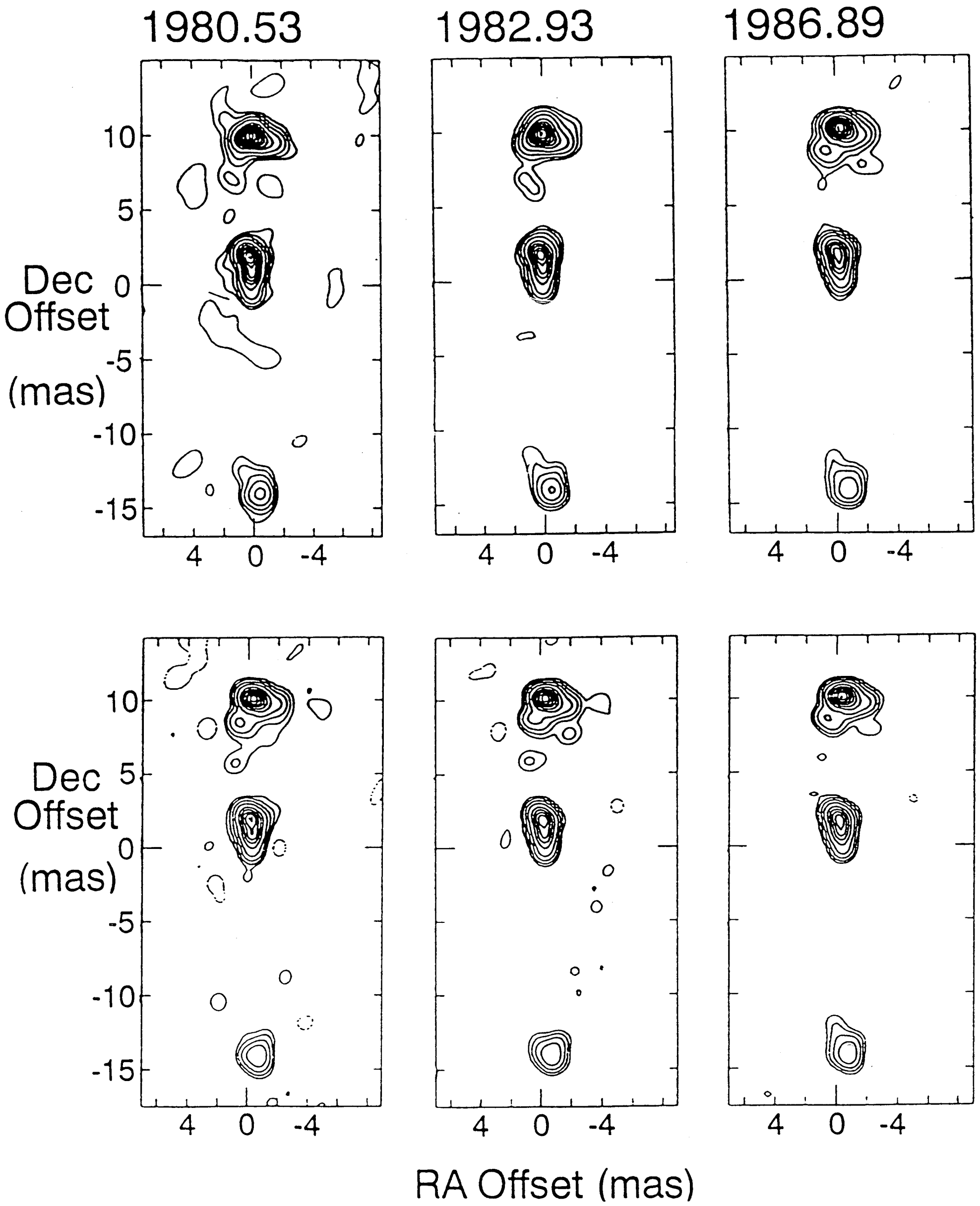

FIG. 5.—5 GHz maps of 0710+439 at each of the three epochs. The top row shows maps made by using all the data at each epoch and making the maps independently. The bottom row shows maps made with exactly the same UV coverage at the epoch, only UV data on baselines and GSTs common to all three epochs were used to make each of the images. In addition, for images on the bottom row, the initial starting model for self-calibration was the best third epoch map (*top right*). In all cases the resorting beam is 1 mas circular. Contour levels are $-5, 5, 10, 20, 40, 80, 120, 160, 200, 240, 280, 320, 360, 400, 440$ mJy beam^{-1}.

A which best fit the first and third epoch data suggests an increase in the AB separation of only 0.02 mas over 6.36 yr, corresponding to a velocity of 0.054 h^{-1} c (assuming $q_0 = 0.5$). In principle an error on this quantity can be calculated rigorously from the dependence of the agreement factor on the shift of A, but it is unclear what number of degrees of freedom (N) should be assumed. If the errors on each point are independent then $N = 23$ and the measured velocity is highly significant. We prefer to estimate the errors directly from Figure 6; if we take a shift of 0.05 mas to have a 1 σ significance then we conservatively estimate 1 σ errors on the velocity of A of 0.14 h^{-1} c. Our final estimate of the motion of A away from B is therefore 0.054 ± 0.14 h^{-1} c; we therefore do not claim a detection of motion, but do claim a 3 σ upper limit of 0.41 h^{-1} c. Note that this limit simply tests the hypothesis that a single component moves bodily and sets limits on this movement. There could be more complex variations in position and shape of components which conspire to keep the closure phase data the same at each epoch. However we believe that such situations are somewhat contrived and unlikely.

Despite the overall evidence of little change there *is* evidence for small changes occurring within the triangles BONN-HSTK-NRAO and BONN-NRAO-FDVS at points away from the full turns in closure phase. Figure 7 shows these two closure triangles in more detail at all three epochs together with the third epoch model. The most significant changes appear within the triangle BONN-HSTK-NRAO between 1300 and 1400 GST. Differences between model and data on

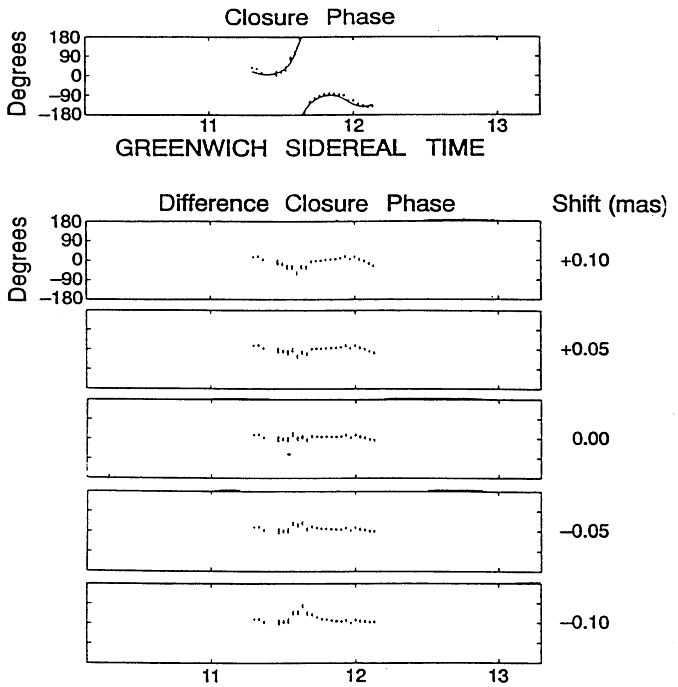

FIG. 6.—Setting a limit on the separation of components A and B between epochs 1 and 3. *Top panel*: the fit of the best third epoch model to the first epoch closure phase data on BONN-NRAO-OVRO, a very close fit is obtained suggesting very small changes in source structure. *Bottom panels*: the difference between the first epoch closure phase and third epoch model data for different shifts in the position of the northern component in the third epoch model. This plot suggests that A has moved relative to B by less than 0.05 mas between epochs 1 and 3.

this baseline are much less at other times, this argues against the differences being due to nonclosing errors due to bandpass mismatch, etc., because these effects are generally constant in time. Based on the error bars of the data points (calculated from the scatter in phase of the 2 s data records emerging from the correlator) the differences between data and model between 1300 and 1400 GST are statistically significant. The closure phase differences and $1\,\sigma$ errors between the data and the third epoch model at the third, second and first epochs are, respectively, 3°.2 ± 1°.0, −7°.3 ± 1°.3, −13°.7 ± 1°.1. These figures are consistent with changes in closure phase at this hour angle between all three epochs. Changes within the triangle BONN-NRAO-FDVS are also significant being respectively for the third, second and first epochs 0°.7 ± 1°.5, 11°.5 ± 1°.9 and 11°.5 ± 2°.7. We have attempted unsuccessfully to fit the multi-epoch closure phase data (both stable and changing triangles) by moving and scaling in flux density the CLEAN components corresponding to each of the three main components. The failure of this process suggests that the closure phase changes are caused by structural changes within a component.

3.4. *Structural Changes*

To identify the nature of the temporal changes within the source we carried out the mapping procedure described in the Appendix, § A3; only data at each epoch with UV coverage common to all three epochs were used and the same starting model was used at all three epochs. The resulting maps (Fig. 5, *bottom row*) all fitted the closure phase data within their respective data sets, including the temporal changes seen on the two affected closure triangles. Figure 5 shows that the shape of the northern component remains very similar from epoch to epoch. There is no evidence to suggest that component A has changed or moved. *This is in contrast to the maps made separately from the full data sets at each epoch which show significant changes* (Conway et al. 1990b); these apparent differences must be ascribed to differences in UV coverage and processing at the three epochs.

Component B shows the most significant changes from epoch to epoch. Figure 8 shows in detail the central component at both the first and third epochs. In the first epoch map there appears to be a secondary maximum to the south of component B while no such maximum is present in the third epoch map. The first epoch map also shows a slightly longer tail extending toward the south. The changes in morphology within B, suggest that this component is responsible for the changes in closure phases. The size of the change in flux density, 40 mJy, is sufficient to explain the observed changes in closure phase. Such a change in the southern part of B would move the centroid of component B toward A by just over 0.05 mas between the first and third epochs. Such a change in centroid position is consistent with our earlier limits on the estimated errors on the separation velocity of A and B.

3.5. *Component Spectra*

The flux densities of the three main components, obtained by integrating rectangular regions on the maps, are listed in Table 2 and Table 3. Included in these tables are the derived

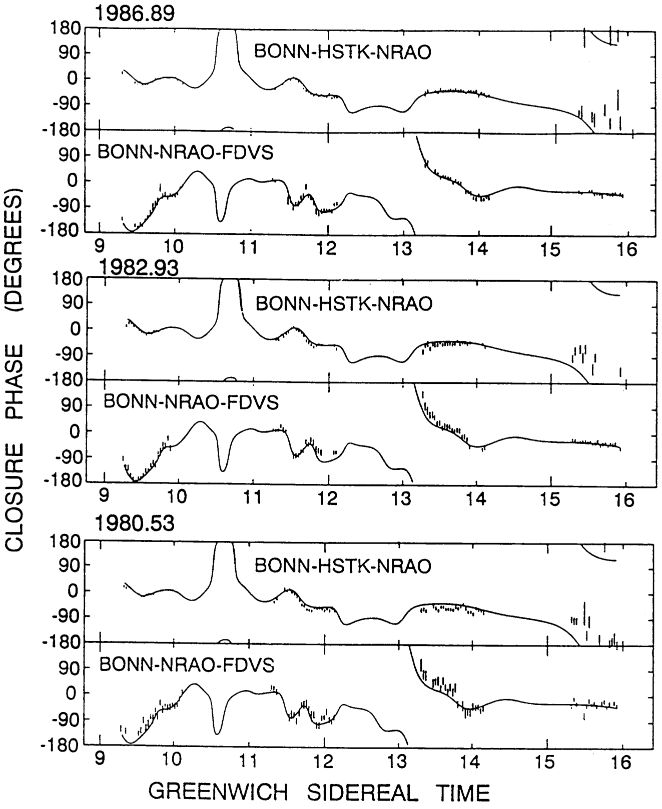

FIG. 7.—VLBI closure phase data showing small temporal changes in 0710+439, at 5 GHz, on two closure triangles, plotted at each of three epochs; note data are only shown at GSTs which are common to all three epochs. Plotted against the data at each epoch is the best third-epoch model. Over the three epochs there are statistically significant changes in closure phase at around 1330 GST.

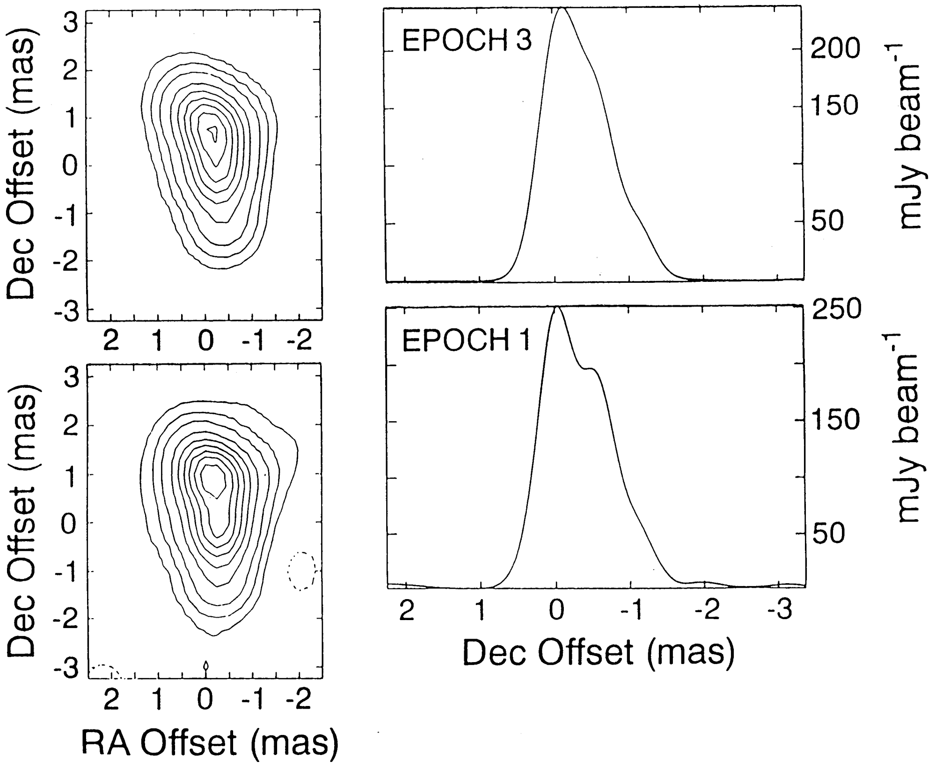

FIG. 8.—Temporal changes within component B of 0710+439. *Top*: third epoch (1986.89) 5 GHz contour map and slice. Peak flux density is 325.3 mJy beam^{-1}. Restoring beam is 1 mas circular, contours at −5%, −2%, 2%, 5%, 10%, 20%, 30%, 40%, 50%, 60%, 70%, 80%, and 90% of peak. *Bottom*: first epoch (1980.53) 5 GHz contour map and slice through component B. Peak flux density is 308.7 mJy beam^{-1}.

spectral indices between 1.66 and 5.01 GHz and between 5.01 and 10.7 GHz. (Spectral index α is defined by $S_\nu \propto \nu^{-\alpha}$.) Although the absolute position of each map is unknown, there can be no ambiguity in identifying the components seen at one frequency with those seen at another, and it is possible to align the maps with sufficient accuracy ($\lesssim 0.5$ mas) to obtain the spectrum of each component. Only when we consider the possibility of spectral variation within the components does the question of image alignment become a significant problem.

Figure 2 shows that the spectrum of component A falls steadily from 1.66 to 10.7 GHz. In contrast the total spectrum of component B rises between 1.66 and 5.01 GHz, and falls between 5.01 and 10.7 GHz, with a maximum at ∼3 GHz. The spectrum of component C is very similar to that of component A. Because of the uncertainties in the absolute calibration, the quoted spectral indices in the fifth and sixth columns of Table 3 can only be believed to within ±0.1. The 5 to 10.7 GHz spectral indices ($\alpha_{5.0}^{10.7}$) of components A and C are both about 0.95, whilst component B is somewhat flatter at 0.68. Within component B there is some evidence for spatial variations in high-frequency spectral index. If we compare the shapes of component B at both 5 GHz and 10.7 GHz (Fig. 4), we find that the peak emission moves toward the south as the frequency is increased. If the images at 5 GHz and 10.7 GHz are aligned so that components A and C coincide without a spectral gradient across either component then we obtain a spectral index of ∼ −0.14 at the southern end of component B. The low fidelity of the 10.7 GHz map means that this result must be treated with caution, but we believe that the properties of the total spectrum also suggest a high-frequency component within component B.

We have attempted to fit the spectra of each of the three components with model spectra expected from homogeneous synchrotron-emitting clouds (van der Laan 1966). Based on their high-frequency spectra we assume high-frequency spectral indices of unity for each of the three components. The model spectra are then completely defined by the values of $\nu_{\max}$, the frequency at which the synchrotron self-absorption occurs, and $S_{\max}$ the flux density at this frequency; these quantities are listed for each component in Table 3. We are able to

TABLE 3

SPECTRAL PROPERTIES OF THE COMPONENTS OF 0710+439

Component	1.66 GHz (Jy)	4.99 GHz (Jy)	10.65 GHz (Jy)	$\alpha_{1.6}^{5}$	$\alpha_{5}^{10.65}$	$S_{\max}$ (Jy)	$\nu_{\max}$ (GHz)	$T_{\nu_{\max}}$ (K)	B_{SSA} (10^{-2} G)
A	1.05	0.529	0.253	0.62	0.95	1.1	1.8	1.1×10^{11}	0.46
B	0.483	0.552	0.330	−0.12	0.68	0.85	2.8	$>1.7 \times 10^{11}$	<0.22
B_1		0.426	0.177		1.15				
B_2		0.129	0.144		−0.14				
C	0.236	0.173	0.081	0.28	0.99	0.28	2.3	3.8×10^{10}	4.8

get good fits with such a model to components A and C but the fit to B is poorer because the VLBI measurements suggest a spectrum broader than can be fitted by a single homogeneous component. Figure 2 also shows the sum of the three model spectra. The fit to the overall spectrum of 0710+439 is inadequate at 1 GHz and below where the model predicts insufficient flux density; it is also inadequate in the range 5–20 GHz. The low-frequency discrepancy is probably due to a largely undetected steep-spectrum component. The 1.6 GHz VLBI map suggests that the northern component A is much larger than at 5 GHz or 10.7 GHz (Table 2). Although some apparent increase in size could be due to optical depth effects in a homogeneous or Gaussian component (Readhead et al. 1983) it seems that an additional component is required to explain these imaging results as well as the spectrum. The fit between 5 and 20 GHz might be improved by reducing the high-frequency spectral index to allow a broader maximum but then too much flux density is predicted at 30 GHz. One could invoke energy-loss mechanisms which cause the spectra to steepen at frequencies $\gtrsim 10$ GHz. A simpler suggestion which requires fewer adjustments is that component B contains a component which peaks at between 8 and 10 GHz. It is clear from the maps at 5 and 10.7 GHz that B has internal structure; this explains the difficulty of fitting B with a simple spectrum and is compatible with the spectral gradient detected on comparing the 5 GHz and 10.7 GHz maps.

3.6. *Physical Parameters*

Tables 2 and 3 list Gaussian fits to the major components of 0710+439 and the derived physical parameters including peak brightness temperature, equipartition magnetic field, equipartition (minimum) pressure and synchrotron self-absorption magnetic field. Also shown in Table 3 is the frequency of peak emission ($\nu_{\max}$) of a simple synchrotron self-absorbed (SSA) spectrum fitted to the measurements of component flux densities at 1.6, 5 and 10.7 GHz as described in § 3.5 and shown in Figure 2. The quantity $T_{\nu_{\max}}$ listed in Table 3 is the estimated brightness temperature at the peak frequency. The component sizes used in this calculation are a geometrical interpolation of the sizes fitted at adjacent frequencies. The peak brightness for A and C are 1.1×10^{11} and 3.8×10^{10} K, respectively. These values are well below the inverse Compton limit of $\approx 10^{12}$ K as is commonly found in compact objects (Scott & Readhead 1977). Brightness temperatures above the inverse Compton limit would imply bulk relativistic motion within A and C. The measured values are consistent with subluminal motions as indicated by the limits set on proper motion (see § 3.3).

Table 2 lists the derived equipartition magnetic field and the corresponding equipartition energy density at each of the observed frequencies (Moffet 1975; Miley 1980). These figures assume a uniform source with a ratio of energy in heavy particles to electrons of unity; they also assume that the filling factor is unity. Magnetic fields can also be derived from the synchrotron self-absorption (SSA) cutoff (Kellermann & Pauliny-Toth 1981) using $\nu_{\max}$ and an estimated size at this frequency interpolated from measurements at adjacent frequencies. Because the estimated magnetic field scales as the fourth power of the angular size, estimated errors in component dimensions of 20% (see Appendix § A1) correspond to errors in estimated magnetic fields of a factor of 3. The SSA magnetic field for component A is only one-tenth of the equipartition field, suggesting that this component is particle dominated, as are the hotspot regions of classical kiloparsec scale radio sources. In contrast, in component C the equipartition and SSA estimates are approximately the same suggesting that this component is close to equipartition.

The "relaxed" nature of component C suggests that we should investigate the possibility that C does not have a current source of energy. One possibility is that A and C are both plasmoids that were ejected from the center of activity (B) some time ago: first C was ejected to the south, then A to the north. If C is older than A this would explain why C is further from B than is A and why C is weaker and closer to equipartition. Another possibility is that there is a beam which flips direction and is currently feeding A whilst that feeding C is switched off. In either case there is no continuous injection of energetic electrons into C. Using the SSA derived magnetic field, we obtain an electron lifetime within C of only 70 yr. However, because this estimated lifetime depends on the component size to the fifth power and the spectral turnover frequency to the sixth power (quantities which we estimate to have inaccuracies of 30% and 50%, respectively) the estimated age can be in error by a factor of 40. Taking these inaccuracies into account we obtain an upper limit for the age of C of about 3000 yr. We emphasize that this upper limit assumes that within C there is no internal electron acceleration. An age of 3000 yr would only require a transverse velocity of $0.07\ h^{-1}\ c$. Such a velocity is consistent with the upper limits on the separation velocity of A from B found in § 3.3, we therefore cannot rule out an unpowered plasmoid model based on electron age and velocity limits. We note that if A and C are powered by presently undetected jets, as are the lobes of kiloparsec scale sources, then the electron age puts no constraint on the age of A or C.

Given the estimated minimum pressures of 10^{-4} dyn cm^{-2} within the main components (which in the case of C is probably close to the true pressure) we can enquire whether the components are confined and if so how. We can exclude the possibility that A and C are freely expanding using the argument presented by Mutel et al. (1985) for compact doubles. Because the lobes would be expanding at the relativistic sound speed (we assume they consist of relativistic plasma) ($c/\sqrt{3}$) there would be a minimum angle the components must subtend at the center of the source which exceeds that actually observed. The above model effectively assumes that the components freely expand into a vacuum. In practice the radio emission will be embedded in a medium whose static pressure and inertia might confine the components. Let us first consider static pressure confinement. The optical spectra of 0710+439 and 2352+495 show narrow line emission similar to that seen in other radio galaxies (§ 2.1). The radio emission on scales of 100 pc or so should therefore lie within the NLR of the host galaxy. To obtain an order of magnitude estimate of the NLR pressure on these scales we use the canonical values derived for AGN nuclei. Optical line properties of AGNs suggest narrow line clouds with typical temperatures of 10^4 K and densities of $10^{4\pm1}$ cm^{-3} (Netzer 1991). In order to confine such clouds an intercloud medium has been suggested having temperature 10^6 K (Krolik & Vrtilek 1984) and hence density $10^{2\pm1}$ cm^{-3}. Taking the above figures, pressures of $10^{-8\pm1}$ dyn cm^{-2} are predicted, insufficient by a factor of 10^4 to confine the radio components by static pressure. We note however that the above pressure estimates generally refer to scales of order 1 kpc and pressures 100 pc from the nucleus are likely to be larger. In addition there is some marginal evidence that densities and pressures within compact doubles are somewhat larger than those in other radio galaxies. For instance the narrow line ratios for the compact double 1934−63 (Fosbury 1990; Penston & Fosbury 1978) suggest pressures of up to 10^{-7} dyn cm^{-3}. However even if cloud densities are a factor of 10 higher in compact doubles than in other radio galaxies it seems unlikely that the NLR pressure can increase by an additional factor of 10^3 between scales of 1000 and 100 pc from the nucleus in order to confine the radio components by static pressure. We therefore rule out static pressure as a means of confining the components.

In contrast it appears that ram pressure could confine the components. Two possibilities exist, in the first the components are expanding spherically but the velocity of expansion is limited by the inertia of the medium. Assuming a medium density equal to that of the intercloud medium we obtain a lower limit of $10^{-1.5\pm0.5}$ c for the velocity of expansion of the components. Given the accuracy of our estimates of component size such small rates of expansion cannot be ruled out by the data. In such a scheme the component could either be supplied with energy from an unseen jet or could be a plasmoid with no energy source. The second possibility is that the components A and C are moving away from the middle component B at such a speed that their leading edges are ram pressure confined. In such a scheme the component must be advancing by at least $10^{-1.5\pm0.5}$ c. Such an advance velocity is well within the limits on proper motions established in § 3.3. In this scheme the rear side of the component would not be confined and there would be free expansion back toward the middle of the source. For this reason in this scheme there must be a continuous injection of energy from a jet to compensate for adiabatic losses.

4. VLBI OBSERVATIONS OF 2352+495

4.1. *Observations*

The source 2352+495 has been observed both at 5 GHz and at 10.7 GHz. At 5 GHz we have three epochs of observations spread over 7 yr. Observations at both frequencies utilized the telescopes of the US VLBI Network and the European VLBI network (EVN) (Table 4). All observations were made in left circular polarization (IEEE convention) and a bandwidth of 1.8 MHz was recorded using the Mark-II format (Clark 1973). The data were cross-correlated with the JPL-Caltech VLBI Processor. The data were processed in the standard manner as described in § 3.1.

4.2. *Evidence of Triple Structure*

The published first epoch 5 GHz map of 2352+495 (Pearson & Readhead 1988) consisted of a bright component (B) which was subdivided into two compact subcomponents; to the north was a weaker component (A). This first-epoch map gave a poor fit to the data and it was clear that a large amount of flux density was unaccounted for. The second-epoch map had a very similar structure. However, with the third epoch data, which contained substantially more short baselines due to the inclusion of four European stations, it was clear that the data could not be fitted adequately by a two component model. Structure at the southern edge of the map was indicated. When a larger map was made, a third southern component denoted by C was found (Fig. 1*b*). Tapered maps revealed this third component (Fig. 9*a*) strongly indicating that most of the missing flux density was contained within the third component. We carried out a number of tests to convince ourselves of the reality of the southern component, including windowing in just the northern and central components, self-calibrating with this model then mapping the short spacing data, but the third component always appeared. On remapping the first two 5 GHz epochs (Fig. 10) and the 10.7 GHz data an improved fit was obtained if the southern component was allowed within the CLEAN windows, an improvement which did not occur if the CLEAN window was placed elsewhere.

4.3. *General Morphology*

Table 5 lists Gaussian parameters for each of the main components within 2352+495 at each frequency. In the case of 10.7 GHz data we do not feel the fits are reliable for components A and C and fits for these components are not given. The parameters at 5 GHz come from using the AIPS task JMFIT to fit Gaussian components to the third epoch image whilst those at 10.7 GHz come from fitting models directly to the UV data. The accuracy of the parameters in the 5 GHz full-resolution maps have been estimated by mapping and fitting simulated data as described in the Appendix, § A1.

We consider the morphology of the outer components first. At full resolution at 5 GHz component A consists of a feature smaller than the resolving beam with flux density 76 mJy. In contrast the tapered map contains over 3 times as much flux density. Feature A is best modeled as two components with two quite different dimensions. The compact part of component A is also revealed by the 10.7 GHz data. A feature of

TABLE 4

JOURNAL OF OBSERVATIONS OF 2353+495

Parameter	5.01 GHz	4.99 GHz	4.99 GHz	10.65 GHz
Epoch	1979.94	1983.93	1986.89	1982.10
Duration (hr)	10	12	3 × 1	11
Antennas[a]	BKGFO	BKGFYO	SJBWKGFYO	BKGO
Maximum baseline ($M\lambda$)	136	136	136	289

[a] S—26 m, Onsala Space Observatory, Onsala, Sweden; J—25 m, Mk II Telescope, Jodrell Bank, Cheshire, UK; B—100 m, Max-Planck-Institut für Radioastronomie, Effelsberg, Germany; W—14 × 25 m, Phased Array, Westerbork Synthesis Radio Telescope, Netherlands; K—36.6 m, Haystack Observatory of the Northeast Radio Observatory Corporation, Westford, Massachusetts; G—42.7 m, National Radio Astronomy Observatory, Green Bank, West Virginia; I—18.3 m, North Liberty Radio Observatory of the University of Iowa, North Liberty, Iowa; F—26 m, George R. Agassiz Station of Harvard University, Fort Davis, Texas; Y—25 m, one antenna of the NRAO Very Large Array, Socorro, New Mexico; O—40 m, Owens Valley Radio Observatory of the California Institute of Technology, Big Pine, California; H—25.9 m, Hat Creek Observatory of the University of California, Cassel, California; P—25.6 m, Dominion Radio Astrophysical Observatory of the National Research Council of Canada, Penticton, British Columbia, Canada.

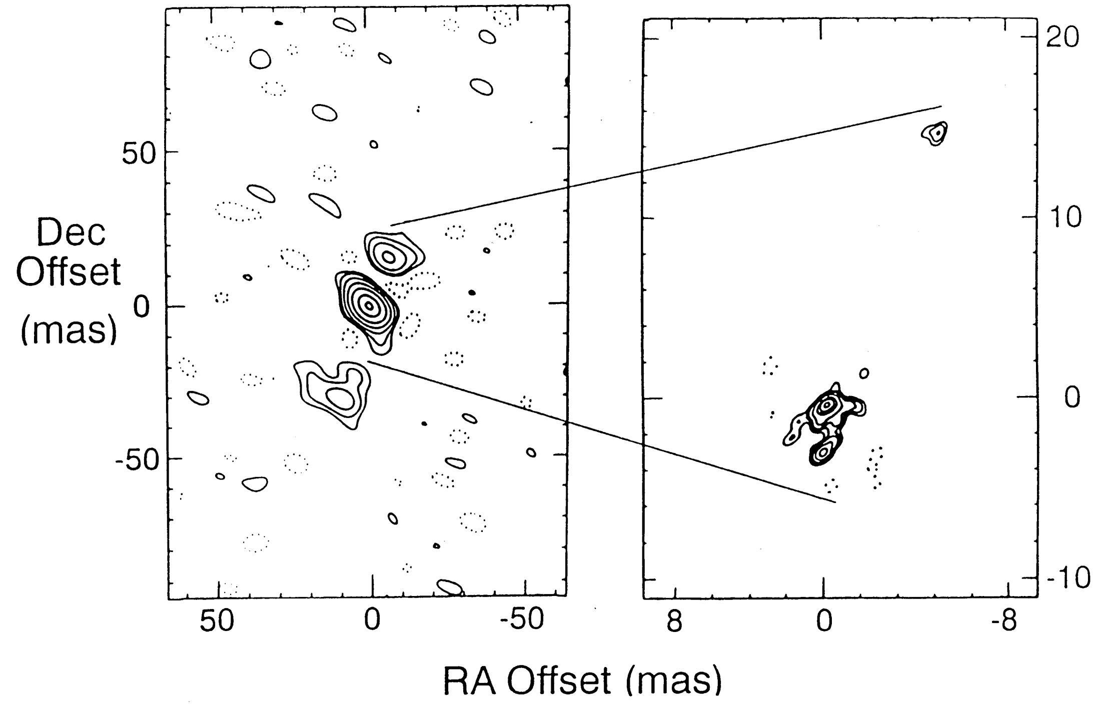

FIG. 9.—Maps of 2352+495 at 5 and 10.7 GHz. (*a*) Tapered 5 GHz map using only the inner 20 $M\lambda$ of UV data. Restoring beam is 9.66 by 6.40 mas position angle 47°9, peak is 1.026 Jy beam^{-1}, contour levels are −2%, 2%, 4%, 8%, 16%, 32%, 64%, and 95% of peak. (*b*) Full-resolution 10.7 GHz map, showing components A and B only, C is detected but is to the south of this field. Restoring beam is 0.7 by 0.5 mas position angle −40°. Peak flux density is 141.2 mJy beam^{-1}. Contour levels are −3%, 3%, 6%, 10%, 20%, 40%, 60%, and 90% of the peak.

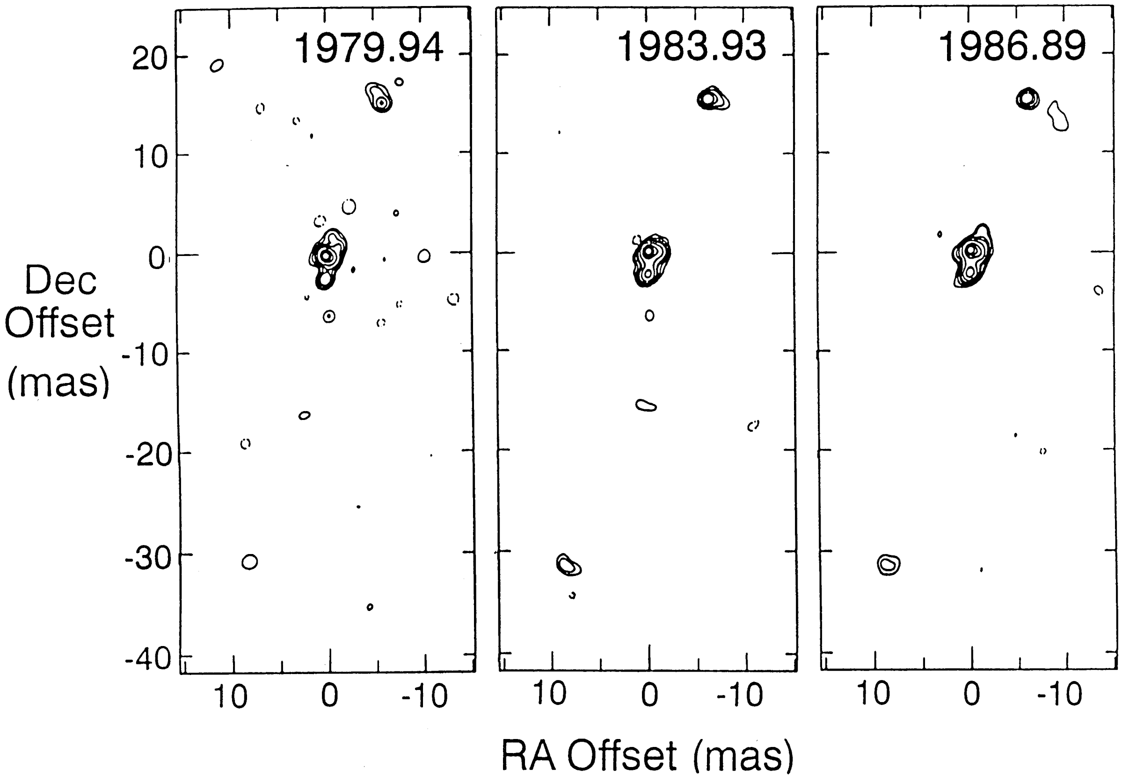

FIG. 10.—Three 2352+495 5 GHz epochs. Restoring beam 1 mas circular. Contours are −6%, −3%, −1.5%, 1.5%, 3%, 6%, 10%, 20%, 40%, 60%, and 80% of the peak. The peaks in each map from left to right are 499, 388, and 307 mJy beam^{-1}, respectively. Note the higher ratio of the flux density of B_1 to B_2 in epoch 1 compared to epochs 2 and 3.

TABLE 5

GAUSSIAN FITTING OF 2352+495

Component	Frequency (GHz)	Flux Density (Jy)	Major (mas)	Minor (mas)	Position Angle	T_B (K)	B_{me} (10^{-2} G)	U_{me} (10^{-4} ergs cm^{-3})
A	4.99	0.076	0.81	0.46	66°	1×10^{10}	5.6	2.9
B_1	4.99	0.62	1.15	1.02	9	2.6×10^{10}	5.7	3.0
B_{1A}	10.65	0.20	0.48	0.30	−58	1.5×10^{10}	12.5	14.5
B_{1B}	10.65	0.40	2.9	1.102	105	1.3×10^{9}	4.0	1.48
B_2	4.99	0.288	1.07	0.46	161	2.8×10^{10}	7.6	5.3
	10.65	0.159	1.05	0.43	−38	3.8×10^{9}	7.1	4.7
C	4.99	0.041	1.51	1.35	57	1×10^{9}	2.1	0.4

largest dimension 0.8 mas is found by model-fitting. Component C is resolved in the full resolution 5 GHz maps (see Fig. 10). At 1 mas resolution it appears weaker (41 mJy) and larger than component A, whilst at EVN resolution in the tapered map (9.7 × 6.4 mas in p.a. 47°9) the flux density is 275 mJy, comparable to that found within A. At the lowest resolution at 5 GHz the ratio of the flux density of A to C is 0.86, while the ratio of the flux density in B to that in the outer components is 2.24. The arm length ratio of the separation between B and C to that between A and B is 1.77. The total angular size is 45.7 mas giving a projected linear size of 106.9 h^{-1} pc.

At 5 GHz most of the flux density (95%) within the middle component B is contained within two compact subcomponents, which are labeled B_1 and B_2 (see Fig. 1*b*). In addition some resolved emission (size of order 2 mas) is indicated close to B_1. In the third epoch 5 GHz map a single Gaussian fit to B_1 shows it to have a size of approximately 1 mas, but this may be an overestimate because of the presence of the resolved emission. In contrast at 5 GHz B_2 appears unresolved (i.e., a fitted dimension less than 0.5 mas) in the east-west direction at all three epochs and just resolved in the north-south direction. The 10.7 GHz mapping (see Fig. 9*b*) and model-fitting suggests a very similar substructure within B to that suggested by the 5 GHz observations. Again there is a basic double structure with more diffuse emission associated with the northern end of B. However, in order to obtain a good fit to the UV data it was necessary to model B_1 as two Gaussians (denoted B_{1A} and B_{1B}) with one Gaussian used to model B_2. All the fitted components were resolved, with the most compact components B_{1A} and B_2 having their minor axes larger than 0.3 and 0.43 mas, respectively.

4.4. *Flux Density Changes within the Central Component*

Maps made from the full data sets at each epoch (Fig. 10) suggest that there is a significant change in the relative brightness of the subcomponents within B, particularly between the first and second epochs. Changes in the source structure should not be unexpected given the variations in total flux seen by Waltman et al. (1991). Figure 11 shows for the first two epochs the observed amplitudes on the baseline BONN-NRAO and the closure phases on the triangle BONN-NRAO-FDVS. Plotted against both data sets is the model which fits the second epoch data. The amplitudes shows a convex feature due to the beating between components B_1 and B_2. Superposed upon this is a more rapid (30 minute period) beating due to component A. The amplitudes show a deeper minimum around 0400 GST in the second epoch compared to the first. Accompanying the amplitude change is a change in closure phase on triangles in which BONN-NRAO is involved (Fig. 11). A plausible explanation for these changes is that one of the subcomponents within B changed in flux density; as indicated in the maps. The size of the change seen within the maps, 75–100 mJy, is consistent with the variations within the multi-epoch UV data.

The data from epochs one and two were also analyzed as described in the Appendix § A3, with exactly the same aperture coverage and starting model. Figure 12 shows maps and slices through component B for each of the resulting images. These slices show that the ratio of flux density within B_1 to that within B_2 decreased by a factor of 1.5 in the 3.99 yr between the two epochs. Possible changes within B are also indicated on comparing the Epoch 2/Epoch 3 map pair. Both examinations of the difference image formed from this pair and Gaussian fitting suggested that the peak brightness of sub-component B_1 decreased by 40 mJy beam^{-1} while that of B_2 stayed constant. The overall flux density of B_1 stayed the same, but the size of

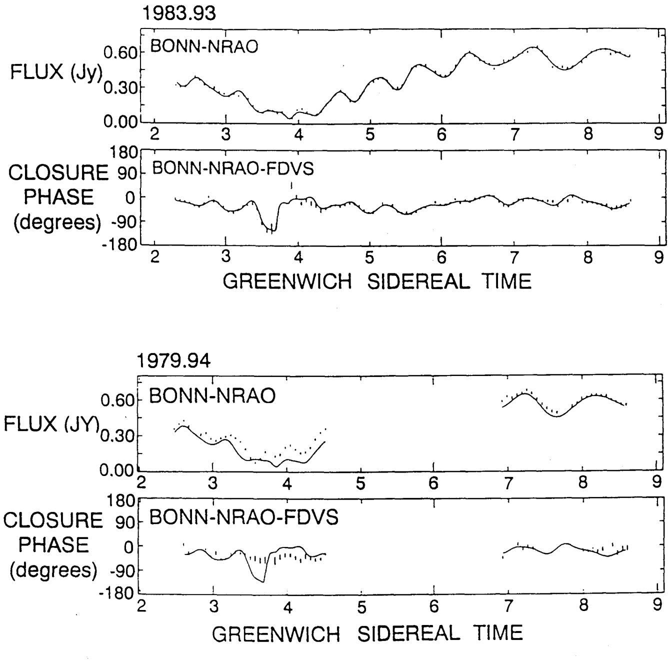

FIG. 11.—Temporal changes in UV data from 2352+495 at 5 GHz between epochs 1 and 2. *Top*: second epoch model plotted against second epoch data. *Bottom*: same model plotted against first epoch data.

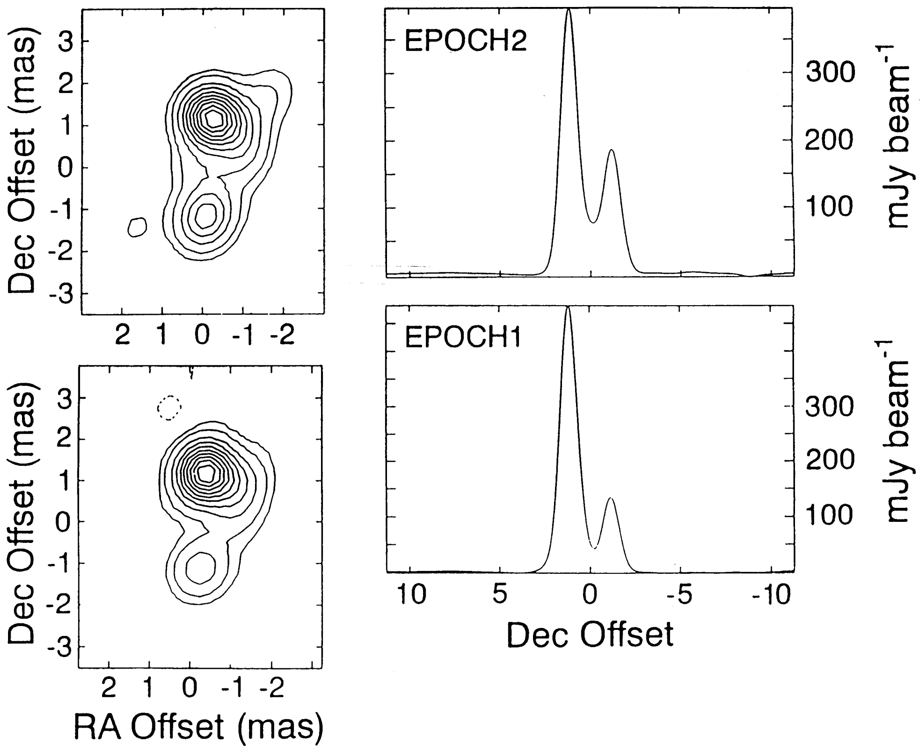

FIG. 12.—Temporal changes within component B of 2352+495. *Top*: Second epoch (1983.93) 5 GHz contour map and slice. Peak flux density is 388 mJy beam^{-1}. Restoring beam is 1 mas circular, contours at −5%, −2%, 2%, 5%, 10%, 20%, 30%, 40%, 50%, 60%, 70%, 80%, and 90% of peak. *Bottom*: first epoch (1979.94) 5 GHz contour map and slice through component B. Peak flux density is 499 mJy beam^{-1}.

the component increased. The errors on these parameter fits due to thermal noise and residual data errors were estimated by shifting each image, adding this shifted image to the original image and refitting the Gaussian. From this method errors of only 2 mJy beam^{-1} were estimated for the peak brightness of B_1 and B_2.

Given the possible errors in overall calibration it is not certain whether the variations occurred within subcomponents B_1 or B_2; however, Figure 10 suggests that B_1 was brighter relative to components A and C in epoch 1 than in epochs 2 and 3. Assuming that A and C did not vary (which seems likely given that their flux density ratio did not change) this suggests that it was B_1 that changed in flux density. However, comparison between maps made at different epochs with exactly the same aperture coverage and starting model is inconclusive, with evidence for both B_1 and B_2 varying with respect to A and C. Analysis of the first epoch map is complicated by the relatively poor quality of the data at this epoch.

4.5. *Component Movements*

We have attempted to set limits on relative component movements, using the technique described in the Appendix § A3, in which maps are made at pairs of epochs using only data *having common UV coverage* and using the same starting model. In the following discussion the first epoch map made using only UV data in common with the second epoch is denoted map E12 while the corresponding second epoch map made with data in common with the first epoch is denoted E21. We will only consider comparisons between epoch 1/epoch 2 and epoch 2/epoch 3 because there is very little common UV coverage between epochs 1 and 3.

First we consider limits on the separation of components A and B_1. Comparison between maps E12 and E21 is difficult because E12 contains relatively large residuals in the region of A which contribute errors in the position of A of order 0.3 mas; we therefore do not believe that the measured change in separation between A and B_1 of 0.6 mas is significant. The epoch 2/epoch 3 map pair made from overlapping coverage (E23 and E32) are of much higher quality and allow useful velocity limits to be set. The Gaussian parameter fits give a decrease in separation of only 0.090 mas over the 2.96 yr between the two epochs, corresponding to a velocity of $-0.42\ h^{-1}\ c$. We believe the errors on the position of A and B_1 are dominated by the additive features in the residuals and remaining reconstruction errors. Based on the size of the fluctuations in the residuals off-source we estimate a 1 σ error of 0.025 mas in the position of A from additive errors alone. Therefore, even if we consider only the additive errors, the detected change is barely significant. We treat the measured shift as an upper limit on the size of any real shift because simulations have shown (see Appendix § A3) that despite using exactly the same starting model any bias toward reducing real motion is likely to be small. We are therefore confident in claiming that the separation velocity of A from B_1 is subluminal.

Next we consider the separation of B_1 and B_2. Gaussian fits give a change in position between maps E12 and E21 (interval 3.99 yr) of B_2 relative to B_1 of 0.097 mas south and 0.072 mas west. Between maps E23 and E32 (interval 2.96 yr) the relative position change of B_2 is 0.050 mas south and 0.070 mas east. The additive errors estimated by the method of adding shifted versions of the maps and refitting Gaussians are less than 0.020 mas for the epoch 1/epoch 2 comparison and 0.010 mas for the epoch 2/epoch 3 comparison. Additive errors alone appear insufficient to explain the apparent changes. Either the changes

1992ApJ...396...62C

are real or they indicate the size of the differential reconstruction error between the epochs. This second possibility seems more likely, there is no evidence for any systematic "signal" of motion within the data sets. The changes are consistent with reconstruction error "noise"; however it is also possible that the measured shifts are real and due to the effects of refractive interstellar scattering (RISS) (see § 4.6).

4.6. *Intrinsic or Extrinsic Variability?*

Measurements of total flux density at 2.3 GHz indicate 10%–15% variability with characteristic time scales less than 6 months (Waltman et al. 1991) and with peak to peak amplitude 200 mJy. At 8 GHz there is also evidence for flux variations although of smaller fractional amplitude. As indicated by our analysis of multi-epoch 5 GHz data (see § 4.4), we believe these variations occur within the compact structure seen within component B.

First we consider whether the variations could be intrinsic to the source. If we assume that the component that is varying is of diameter smaller than 1 lt-yr and has flux of order 200 mJy we infer a brightness temperature of $2.7\ h^{-2} \times 10^{12}$ K at 2.3 GHz. This is larger than the inverse Compton limit of 10^{12} K (Kellerman & Pauliny-Toth 1969) implying some relativistic motion within the varying component. An upper limit on the X-ray flux of 0.31 μJy at 1 keV, measured by *HEAO-1* (quoted by Biermann et al. 1987) can be used together with variability measurements to set a limit on the Doppler boosting factor. We assume an optically thin spectral index of 1.0, consistent with the overall high-frequency spectrum and the spectral index of B (see § 4.7). We note that the derived beaming factor only varies at the tens of percent level for α in the range 0.5 to 1.0. Somewhat more important is the assumed frequency of synchrotron self-absorption. With VLBI observations at only 5 and 10.7 GHz we have yet to observe this turnover directly although it must be below 5 GHz. However, the estimate of the beaming factor is minimized if the varying 200 mJy component observed at 2.3 GHz peaks at that frequency so we take 2.3 GHz as the turnover frequency. The formula given by Marscher (1983) for predicted inverse Compton X-ray flux assumes a uniform spherical source of diameter θ. Setting $\theta = 0.13\ h^{-1}$ mas appropriate for a diameter of 1 lt-yr we obtain that $\delta > 5.3\ h^{-5/3}$, where $\delta = \gamma^{-1}(1 - \beta \cos \phi)^{-1}$. γ is the bulk Lorentz factor, β the velocity in units of the speed of light, and ϕ the angle to the line of sight. If the source diameter is 2 lt-yr then still $\delta > 1.7\ h^{-5/3}$, therefore even being conservative it appears that an intrinsic origin to the variability requires bulk relativistic motion with the varying component B. For $\theta = 1$ lt-yr minimum values of γ are 8.4 and 6.5 for $h = 0.5$ and $h = 1$, respectively, while if $\theta = 2$ lt-yr then minimum values of γ are 6.4 and 1.2, respectively.

Given that the observed variability at 2.3 GHz is larger than at 8 GHz and that the Galactic coordinates of 2352+495 are $b_{\rm II} = -12^\circ\!.0$ and $l = 113^\circ\!.7$, this suggests we should investigate refractive interstellar scattering (RISS) as the origin of the variability seen within component B (see § 4.4). The expected scintillation index (i.e., fractional flux variation $m = \overline{\delta I}/I$) depends on (a) the ratio of intrinsic to diffractive scattering size and (b) the shape of the spatial spectrum of turbulence. In the following, we will assume a power-law form with a finite high wavenumber cutoff $[P(q) \propto q^{-\alpha} \exp - ql_0/2)$, where l_0 is the inner scale.

For a "shallow" power-law spectrum ($2 < \alpha < 4$), the expected scintillation index depends on whether the intrinsic source angular size (θ_o) is greater than the diffractive scattering size (θ_s). We can estimate the minimum angular size for incoherent emission using the inverse Compton limit for the brightness temperature $T_B < 10^{12}$ K and the measured flux densities; these are $\theta_0 = 0.12$ and 0.17 mas for components B_1 and B_2, respectively. The expected scattering sizes at 5 GHz can be obtained using (e.g., Cordes 1984)

$$\theta_s = 3.8(SM)^{0.6} \text{ mas} ,$$

where the strength of turbulence is given by the scattering measure ($SM = C_n^2 L$ m$^{-20/3}$ kpc) and we have taken the Kolmogorov value $\alpha = 11/3$ for convenience. Cordes et al. (1991) have recently analyzed over 200 lines of sight of scattered sources to determine the galactic distribution of turbulence. For the range $100° < l < 180°$ and $b > 10°$ there are eight measurements, all of which produce scattering measures in the range $10^{-4} < SM < 10^{-3}$ m$^{-20/3}$ kpc. Hence we expect a diffractive scattering size at 5 GHz of $0.02 < \theta_s < 0.06$ mas in this region, much smaller than the minimum intrinsic size. Under the assumption $\theta_0 > \theta_s$ and using $\alpha = 11/3$, the expected scintillation index at 5 GHz is (e.g., Coles et al. 1987)

$$m = 0.13(SM)^{1/2} L^{-1/6} \theta_0^{-7/6} ,$$

where L is the distance to the scattering screen in kpc and θ_0 (defined by the $1/e$ visibility) is in units of mas. For scattering measures in the range given above, the scintillation index is $m \lesssim 0.05$ for both B_1 and B_2. The required change in relative flux density between B_1 and B_2 (see Fig. 12) would require at minimum $m \approx 0.20$ for both subcomponents, hence it does not appear that the observations could be explained by normal scattering.

It is possible however that the line of sight to the source has anomalously strong scattering. The source is positioned near the maximum of a steradian-sized rotation measure feature dubbed region A (Simard-Normandin & Kronberg 1980). At the position of 2352+495 the rotation measures detected are amongst the largest detected in the sky. The region is surrounded by the continuum feature Loop III (Berkhuijsen, Haslam, & Salter 1971). Heiles (1984) considers the physical properties and nature of the region and concludes that it is probably a bubble of ionized gas with diameter 1 kpc formed from repeated supernova explosions and stellar winds. Also, Fiedler et al. (1992) point out that the line of sight to 2352+495 passes close to an infrared knot. They suggest that the flux variations they detected at epoch 1984–5 (which they identify with an "extreme scattering event") might have been caused by a shock-driven density enhancement associated with the IR knot. If we assume the measured sizes are due to scattering, the inferred scattering measures are $SM = 0.10$ (B_1) and 0.03 (B_2). While this is much higher than other measurements in this direction, there are some heavily scattered sources which have similar values of SM (Cordes et al. 1992). For a source size which is less than the scattering disk, the scintillation index will depend on the size of the inner scale. We expect $m \gtrsim 0.1$ only if $l_0 \sim \theta_0 L \sim 10^{12-13}$ cm (Coles et al. 1987). Recent evidence from VLBI angular broadening measurements (Spangler & Gwinn 1990; Molnar et al. 1992) suggest that the inner scale in the ISM is probably much smaller, $l_0 \sim 10^{7-8}$ cm. For this case, the scintillation index is much less than unity unless the intrinsic source size is $\theta_s < r_d/L \sim 10^{-2}$ mas. This is only satisfied in the case of pulsars.

We next consider "steep" turbulence spectra ($4 < \alpha < 6$). Although the scintillation index will likely be large (e.g.,

$m \sim 0.5$ for $\alpha = 4.3$, Romani, Narayan, & Blandford 1986), there will in addition be a substantial differential angular wander between components B_1 and B_2 on a time scale $t \sim r_f/v \sim 1$ month, where $r_f = \theta_s L \sim 10^{12-13}$ cm is the refractive or "multipath" scale and $v \sim 10^7$ cm s^{-1} is the bulk velocity across the line of sight. The rms differential angular wander for two closely spaced components separated by angle Θ for $\alpha > 4$ is (Rickett & Coles 1988)

$$\langle \delta\Theta \rangle = \theta_s \left(\frac{\Theta}{\theta_s}\right)^{(\alpha-4)/2} .$$

Where θ_s is the diffractive scattering size as defined above. For $SM \sim 10^{-3.5}$ ("normal" scattering), $\theta_s \sim 0.04$ mas, and $\Theta = 3.5$ mas, $\langle \delta\Theta \rangle$ is larger than the observed motion of 0.09 ± 0.02 mas for all $\alpha > 4.2$. For much larger values of SM ("anomalous" scattering), the limit is even more stringent.

We conclude that the observed variability is unlikely to be RISS unless (a) the turbulence spectrum is shallow ($\alpha < 4$) with a large inner scale ($l_0 \gtrsim 10^{-2}$ cm) and anomalous scattering measure ($SM > 10^{-2}$ m$^{-20/3}$ kpc), or (*b*) the turbulence is steep but constrained to a narrow range of spectral index ($4.0 < \alpha < 4.2$). Under the alternative explanation that the variability is intrinsic we have found that we require relativistic flow within B. Even though we cannot at present determine whether the observed variability is intrinsic or extrinsic, we note that both mechanisms require that the most compact structure be found within the varying component; namely component B.

4.7. *Component Spectra*

Table 6 gives estimates of 5 GHz and 10.7 GHz flux densities of components measured from 1 mas resolution images at each frequency together with the derived spectral indices. The outer components A and C have spectral indices of approximately unity, similar to the case for 0710+439 (see § 3.5). Within B the northern subcomponent (B_1) apparently has a somewhat flatter spectral index of 0.41, while B_2 is steep with index 1.13. We must be cautious, however, in interpreting these spectral indices because we know there is variability within B (see § 4.4). The time interval between the 10.7 GHz map and the nearest 5 GHz map is 1.83 yr, longer than the variability time scale of less than 6 months (Waltman et al. 1991). Given the amplitude of the detected variability, the derived spectral indices within B could be in error by as much as 0.3.

Figure 3 shows the total spectrum of 2352+495 and the flux density seen in each of the three main components at 5 GHz and 10.7 GHz. The flux densities were measured from maps with resolutions of 2.5 mas at each frequency. At neither frequency is all the single dish flux density contained within the images and it appears that the diffuse components associated with A and C are not well modeled in either image. Without spectral information about the separate components at a lower frequency such as 1.6 GHz it is impossible to carry out a decomposition of the total spectrum as was done for 0710+439.

TABLE 6

SPECTRAL PROPERTIES OF THE COMPONENTS OF 2352+495

Component	4.99 GHz (Jy)	10.65 GHz (Jy)	$\alpha_6^{2.8}$
A	0.076	0.033	1.11
B_1	0.532	0.388	0.41
B_2	0.278	0.118	1.13
C	0.035	0.016	1.03

The high-frequency spectral indices of the diffuse emission within A and C can be roughly estimated by subtracting the flux density of the 5 GHz and 10.7 GHz maps from the single dish flux densities at these frequencies. This procedure yields an estimate for the average spectral index of the diffuse features within A and C of about unity. Taking the total flux density within the diffuse components at 5 GHz to be about 0.5 Jy implies that the spectra of both A and C must be self-absorbed above 500 MHz in order to avoid conflict with the total spectrum of the source. Extrapolating the spectrum of component B to lower frequency likewise suggests that, in order to be consistent with the single-dish spectrum, the spectral turnover must be above 1 GHz. It is clear that in order to fully understand the spectral behavior of this source VLBI observations are required at lower frequencies, particularly at 1.6 GHz.

4.8. *Physical Parameters*

From the Gaussian parameter fits at each frequency (see § 4.3) values of the physical parameters, brightness temperature, equipartition magnetic field strength, and minimum pressure were derived as shown in Table 5. As was the case for 0710+439 (see § 3.6) the brightness temperatures of A and C are well below the inverse Compton limit of 10^{12} K and so there is no need to invoke relativistic bulk motions of A or C, a result consistent with the subluminal limits on apparent component motions quoted in § 4.5. As with 0710+439 we believe that the smaller fitted dimensions of the subcomponents within B are only upper limits and so the quoted brightness temperatures for these components are only lower limits. The equipartition magnetic field and the minimum pressure were derived according to the equation given by Miley (1980) using the same assumptions as for 0710+439 (see § 3.6). The equipartition fields and pressures derived are very similar to those found in 0710+439 (see Table 3) and within the two components of compact double sources (Mutel, Hodges, & Phillips 1985). Similar reasoning to that described in § 3.6 leads us to believe that the components are not undergoing free expansion but are confined. Assuming typical NLR pressures and densities, static pressure confinement is not feasible, but ram pressure confinement is possible if the velocity of advance of A or C is greater than about 0.1 *c*, which is consistent with the proper motion limits (see § 4.5).

5. DISCUSSION

Both 0710+439 and 2352+495 have a strikingly similar triple structure. The similarities in morphology, spectra, and kinematics strongly suggest a common physical origin for the morphology of these two sources. Based on the relative compactness of the middle components, their flatter spectrum, and their variability there is strong evidence that in both sources these components are associated with the center of activity. In contrast, for the outer components, the morphologies and estimates of internal pressures are consistent with these features being ram confined "micro-lobes" where the jet terminates within the NLR of the galaxy. The subluminal limits set on the separation velocity between the outer components and the middle component are consistent with this scenario. Overall these sources show a symmetric structure. These sources are clearly different from the vast majority of nuclei in powerful extragalactic radio sources in which there is a one-sided jet with a flat-spectrum core at one end.

It is unclear whether these compact triple sources represent a new type of object or, alternatively, whether they are related to the compact double and GPS sources. Many of the optical and radio properties (see § 2) are similar to those found amongst the compact double class and GPS sources including their optical and radio polarization, optical and radio spectrum properties, low variability, and lack of detectable extended radio structure (Hodges & Mutel 1987; Rudnick & Jones (1982); O'Dea, Baum, & Stanghellini 1991). Given their observational similarities we should consider the possibility that in the triples 0710+439 and 2352+495 we are seeing the overall structure of "compact double" sources clearly for the first time. It is notable that Pearson & Readhead (1988) failed to find the third component in 2352+495 which was classified as a double. The source 0710+439 was likewise provisionally classified as a compact double (Pearson & Readhead 1988) based on the definition of Hodges & Mutel (1987) because almost 90% of the flux density originated within two components of almost equal brightness. We note parenthetically that at the time of the above classifications the unusual structure of 0710+439 was recognized and the possibility that "compact double" sources in general might actually have triple structures was seriously considered. A completely different possibility, if true doubles do exist, is that compact triples are related sources in which for some reason the center of activity is unusually prominent.

If the outer components of the triples are the sites at which the jets from the central engine terminate then these sources could be young sources in which the jet has not yet plowed its way out of the dense nucleus (Hodges & Mutel 1987; Carvalho 1985). Note that the fact that the central component is not situated precisely between the two outer components (the two sources have arm length ratios of 1.9 and 1.8, respectively) may mean that there are inhomogeneities in density of the NLR gas of order a factor of 3.5 along opposite lines of sight from the central engine. Alternatively such an arm ratio might indicate that the average advance speed of the jets is dominated by collisions with narrow-line clouds as suggested by O'Dea et al. (1991). Given time the compact triples might evolve into the larger triples seen amongst CSS sources (Spencer et al. 1989; Fanti et al. 1990) which themselves might evolve into classical FRII radio sources (Hodges & Mutel 1987). The ratio of minimum stored energies within the two compact triples and classical double sources such as Cygnus A is about 5×10^5 [Cygnus A has approximately 6.3×10^{59} ergs (Hargrave & Ryle 1974) while the minimum energy is 1.2×10^{54} ergs for 0710+439 and 2.6×10^{53} ergs for 2353+495]. Such a ratio would be consistent with an evolutionary model if the stored energy were roughly proportional to age and linear size.

Although in both sources the middle component B is the best candidate to be associated with the central engine, its properties are different from those of the "cores" seen in superluminal core-jet sources. In both sources B is elongated along the jet axis, actually showing double structure in the case of 2352+495. Unlike in classical superluminal sources the subcomponents within B in 2352+495 appear to be resolved at 10.7 GHz (see § 4.3), although this requires confirmation. In addition, although they have flatter spectral indices than A or C the spectra of the B components are not as flat as those of the cores within classical core-jet sources. Instead, the total spectrum of B is to first order consistent with a simple self-absorbed component with a high frequency spectral index of unity (Figs. 2 and 3). Although in both sources there is some evidence that a subcomponent within B is "flat" between 5 and 10.7 GHz (see § 3.5 and § 4.7), in both cases their spectra must steepen before 30 GHz in order to be consistent with the measured total flux density. These subcomponents could therefore be simple self-absorbed subcomponents peaking between 5 and 10.7 GHz. However more observations at different frequencies are required to definitely determine the spectra of the B components. In particular observations at mm wavelengths such as those presented by Steppe, Salter, & Saikia (1990) would be useful in ruling out flat subcomponents within the B components. A number of interpretations of the unusual morphologies within the B components are possible, including that the subcomponents within B are standing or slowly moving shocks near the bases of two oppositely directed jets. Alternatively one end of B could correspond to the central engine while the rest of the emission could come from an intrinsically one-sided or Doppler boosted jet.

If real compact doubles exist in which the two components can be unambiguously identified as regions where oppositely directed jets terminate, and not be misidentified triples as was originally the case for 0710+439 and 2352+495, we must try to understand why some sources show prominent central components while others do not. Several possibilities exist, including (1) a different type of "engine" in the two types of source; (2) a different environment making the base of the jet visible in the case of the triples; (3) nuclear activity is a transient phenomena: triples are in the active state, while doubles are inactive; (4) the flow is relativistic and the compact triples are doubles seen close to the line of sight, so that the core emission is Doppler enhanced (Conway et al. 1990b, c). In addition to the fact that the middle components do not have the same properties of the beamed superluminal cores this last "unification" of doubles and triples is probably ruled out on statistical grounds. First, the "parent population" of compact doubles is rather small, containing only about half a dozen clear cases compared to the two triples detected, and secondly there appear to be no intermediate cases whose central regions have flux density ratios to the extended components larger than 10^{-2} (the limit set by their nondetection in the doubles) and greater than unity in the case of 0710+439 and 2352+495. Despite these apparent problems larger number statistics would probably be required to certainly reject the beaming hypothesis.

Whatever their nature, the compact triples 0710+439 and 2352+495 are striking in showing a highly symmetric structure in contrast to the majority of VLBI radio sources. The identification of this new morphological class suggests that the full range of phenomena in powerful active galaxy nuclei has yet to be identified and that present and future surveys are likely to hold further surprises.

We thank the United States VLBI Network, the European VLBI Network, the Max-Planck-Institut für Radioastronomie, the Dominion Radio Astrophysical Observatory, and the staffs of the participating observatories for making the observations possible. The work was supported in part by the NSF via grants AST-8814554 to the Owens Valley Radio Observatory, AST-8919386 to the University of Iowa and via its support of the Haystack Observatory and the George R. Agassiz Station. The National Radio Astronomy Observatory is operated by Associated Universities, Inc., under contract with the National Science Foundation.

APPENDIX

ESTIMATING IMAGE RELIABILITY AND TEMPORAL CHANGES

A1. ESTIMATING RELIABILITY WITH SIMULATED DATA

A serious problem with the astrophysical analysis of VLBI maps is that there is much more freedom in making images than is the case of arrays such as the VLA. These differences are due to the fact that the latter instrument produces calibrated phases, well calibrated amplitudes, and generally has much better aperture coverage. Despite these problems, images are made from incomplete VLBI data using nonlinear deconvolution algorithms and self-calibration methods. The inevitable differences between the resulting image and the true image we will describe as "reconstruction errors." To estimate the size of these errors in our maps of 0710+439 and 2352+495 we carried out the following procedure. (1) Each map was parameterized as a model of 4 or 5 Gaussian components. (2) Simulated data were then generated by the Caltech VLBI program FAKE for aperture coverages matching those used in the real observations. The simulated data contained realistic additive Gaussian noise, random antenna-based phase errors and time-varying amplitude calibration errors of order 10%. (3) The simulated data were processed in a manner as similar as possible to the real data. (4) Finally, the resulting maps were compared with the input models and the reconstruction errors were estimated.

Although using a Gaussian model in the above procedure cannot be guaranteed to represent the "true" source we note that we are only aiming to estimate the reconstruction errors in a *similar* source with the same general structure (i.e., number, sizes, and approximate flux density of components). The above procedure cannot take account of effects not included in the simulation such as bad data or nonclosing phase errors on individual baselines. In general such errors scatter flux density around the image causing increased residual errors off-source. In most of our maps the expected thermal noise is achieved off-source and so we do not believe that data errors are a significant source of reconstruction errors. Even when such additive errors are significant, simulations show that such additive errors are not, to first order, amplified by deconvolution (Conway, Cornwell, & Wilkinson 1990a). The total errors in the CLEAN map can therefore be estimated to be equal to the sum of the errors from the imaging simulations and the additive errors.

The results of the mapping simulations suggest that the relative positions of the major components in each source can be trusted to between $\frac{1}{20}$ and $\frac{1}{7}$ of a beam (i.e., 0.05 and 0.15 mas at 5 GHz) depending on the epoch. The relative flux densities of components are accurate to 10%–15%. Structure within the components is less accurately determined. The separation between the subcomponents B_1 and B_2 of 2352+495 (which are approximately 2 mas apart) has errors of between 0.1 and 0.2 mas. Sizes of components larger than half the formal resolution were accurate to better than 20%.

A2. COMPARISON OF MULTI-EPOCH DATA

Given the ambiguities of the imaging process, deciding whether changes actually occur in source structure is best tackled by direct comparison of the *data* at different epochs. Comparing the closure phases is the most reliable approach because unlike amplitudes they are not affected by errors in calibration. Systematic errors in closure phase introduced in correlation are estimated to be less than one degree.

Unfortunately such direct comparison is complicated by the need to interpolate the closure phases over time so that we can compare data at the same GST from different epochs. We must also take into account precession which affects the exact aperture plane coverage and source orientation and hence the observed data at a given GST. Precession effects for 0710+439 and 2352+495 over 7 yr give rise to changes of approximately 31 s in RA, 30″ in declination and 0°.5 in source orientation. Finally we must take account of the differences in aperture coverage because of the slightly different frequencies of observation at each of the three different epochs (by 1 part in 2500, see Tables 1 and 2). The additional effects due to the differences in source structure with frequency are totally negligible over the ranges of frequency used (Conway et al. 1990a). To circumvent these problems we first found a CLEAN component model which fitted the closure phase data at the second epoch under consideration. Model closure phases for the first epoch data were then calculated from this model, using the appropriate source orientation and aperture coverage at the time and frequency of observation of the first epoch. Careful comparison of the model data and the observed first epoch closure phase could then be carried out in order to search for possible changes in source structure. In this technique the use of the CLEAN model allows us to interpolate between the very slightly different aperture coverages at the two epochs. Given the very small differences in coverage, this interpolation should be good to high accuracy. The above technique of closure phase comparison was used in § 3.3 to set sensitive limits to motions within 0710+439.

A3. ESTIMATING STRUCTURAL CHANGES FROM MULTI-EPOCH MAPPING

Although the method outlined above is good at detecting changes, it cannot directly determine the nature of any structural changes which do occur. Comparison of maps made separately at each epoch is in general a poor method of determining these changes because of the different aperture coverages and details of processing at each epoch. Instead the following method was used to compare data at pairs of epochs. First, data sets at each epoch were created with data only on baselines and GST ranges common to both epochs. To ensure the same processing at each epoch these data were then mapped starting with the same best CLEAN model as the input self-calibration model. Solutions for phase and overall antenna based amplitude errors were carried out. The model created after inverting and CLEANing the resulting data was used as the starting point for a second cycle of self-calibration and mapping. After a number of cycles a final map was produced at each epoch. Differences between epochs were then searched for by taking the differences between final maps at each epoch. This technique is very similar to that employed by Masson (1986) on VLA data.

The above procedure limits the differences between the final images at each epoch, so that we could be confident that any differences which remained were required by the data. It could be argued that the initial self-calibration of all the different data sets against the same starting model could potentially remove real changes which occurred between epochs. To quantify this biasing effect simulations were carried out in which FAKE data containing realistic thermal noise and phase errors were created with a four-Gaussian model of the source 2352+495. Components A and B_1 within this model had a separation of 17.07 mas. The data were processed as described above using a starting model with the components having a separation of 16.77 mas. The position of the components in the final map had a separation of 17.00 ± 0.02 mas. A bias error of only -0.07 mas was created by using a self-calibration model in which the separation was some 0.3 mas less than in the true source.

REFERENCES

Baum, S. A., O'Dea, C. P., Murphy, D. W., & de Bruyn, A. G. 1990, A&A, 232, 19

Berkhuijsen, E. M., Haslam, C. G. T., & Salter, C. J. 1971, A&A, 14, 252

Biermann, P. I., Kuhr, H., Snyder, W. A., & Zensus, J. A. 1987, A&A, 185, 9

Bridle, A. H., Kesteven, M. J., & Brandie, G. W. 1977, AJ, 82, 21

Burbidge, G., & Crowne, A. H. 1979, ApJS, 40, 583

Carvalho, J. C. 1985, MNRAS, 215, 463

Clark, B. G. 1973, Proc. IEEE, 61, 1242

Cohen, A. M., Porcas, R. W., Browne, I. W. A., Daintree, E. J., & Walsh, D. 1977, MmRAS, 84, 1

Cohen, M. H., et al. 1975, ApJ, 201, 249

Coles, W. A., Frehlich, R. G., Rickett, B. J., & Codona, J. L. 1987, ApJ, 315, 666

Conway, J. E., Cornwell, T. J., & Wilkinson, P. N. 1990a, MNRAS, 246, 490

Conway, J. E., Pearson, T. J., Readhead, A. C. S., & Unwin, S. C. 1990b, in Parsac Scale Radio Jets, ed. J. A. Zensus & T. J. Pearson (Cambridge: Cambridge Univ. Press), 167

Conway, J. E., Unwin, S. C., Pearson, T. J., Readhead, A. C. S., & Xu, W. 1990c, in Compact Steep Spectrum and GHz-Peaked Spectrum Radio Sources, ed. C. Fanti, R. Fanti, C. P. O'Dea, & R. T. Schilizzi (Bologna: Consiglio Nazionale della Ricerche, Istituto di Radioastronomia), 157

Cordes, J. M. 1984, in IAU Symp. 110, VLBI and Compact Radio Sources, ed. R. Fanti, K. Kellermann, & G. Setti (Dordrecht: Reidel), 303

Cordes, J. M., Spangler, S. R., Weisberg, J. M., & Ryan, M. 1992, ApJ, submitted

Cornwell, T. J., & Wilkinson, P. N. 1981, MNRAS, 196, 1067

Fanaroff, B. L., & Blake, G. M. 1972, MNRAS, 157, 41

Fanti, R., Fanti, C., Schilizzi, R. T., Spencer, R. E., Redong, N., Parma, P., van Breugel, W. J. M., & Venturi, T. 1990, A&A, 231, 333

Fiedler, R. L., et al. 1987, ApJS, 65, 319

Fiedler, R. L., Pauls, T., Johnston, K. J., & Dennison, B. 1992, ApJ, submitted

Fosbury, R. A. E. 1990, in Compact Steep Spectrum and GHz-Peaked Spectrum Radio Sources, ed. C. Fanti, R. Fanti, C. P. O'Dea, & R. T. Schilizzi (Bologna: Consiglio Nazionale delle Ricerche, Istituto di Radioastronomia), 197

Galt, J. A., & Kennedy, J. E. D. 1968, AJ, 73, 135

Gregorini, L., Mantovani, F., Eckart, A., Biermann, P., & Witzel, A. 1984, AJ, 89, 323

Hargrave, P. J., & Ryle, M. 1974, MNRAS, 166, 305

Heiles, C. 1984, in IAU Colloq. 81, The Local Interstellar Medium, ed. Y. Kondo, F. C. Bruhweiler, & B. D. Savage (NASA CP 2345), 263

Hodges, M. W., & Mutel, R. L. 1987, in Superluminal Radio Sources, ed. J. A. Zensus & T. J. Pearson (Cambridge: Cambridge Univ. Press), 168

Kapahi, V. K. 1981, A&AS, 43, 381

Kellermann, K. I., & Pauliny-Toth, I. I. K. 1969, Astrophys. Lett., 155, L71

———. 1973, AJ, 78, 828

———. 1981, ARA&A, 19, 373

Krolik, J. H., & Vrtilek, J. M. 1984, ApJ, 279, 521

Kühr, H., Witzel, A., Pauliny-Toth I. I. K., & Nauber, U. 1981, A&AS, 45, 367

Lawrence, C. R., Pearson, T. J., Readhead, A. C. S., & Unwin, S. C. 1986, AJ, 91, 494

MacLeod, J. A., Swenson, G. W., Yang, K. S., & Dickel, J. R. 1965, AJ, 70, 756

Marscher, A. P. 1983, ApJ, 264, 296

Masson, C. R. 1986, ApJ, 302, L27

Miley, G. 1980, ARA&A, 18, 165

Moffet, A. T. 1975, in Galaxies and the Universe, ed. A. Sandage, M. Sandage & J. Kristian (Chicago: Univ. Chicago Press), 211

Molnar, L. A., Mutel, R. L., Reid, M. J., & Johnston, K. J. 1992, ApJ, submitted

Mutel, R. L., Hodges, M. W., & Phillips, R. B. 1985, ApJ, 290, 86

Netzer, N. 1991, in Active Galactic Nuclei (1990 SAAS-FEE lectures), ed. J. J.-L. Courvoisier & M. Mayor (Berlin: Springer), 57

O'Dea, C. P., Baum, S. A., & Morris, G. B. 1990, A&AS, 82, 261

O'Dea, C. P., Baum, S. A., & Stanghellini, C. 1991, ApJ, 380, 66

Pauliny-Toth, I. I. K., Witzel, A., Preuss, E., Kühr, H., Kellermann, K. I., Fomalont, E. B., & Davis, M. M. 1978, AJ, 83, 451

Peacock, J. A., & Wall, J. V. 1981, MNRAS, 194, 331

Peacock, J. A., Perryman, M. A. C., Longair, M. S., Gunn, J. E., & Westphol, J. A. 1981, MNRAS, 194, 601

Pearson, T. J. 1991, BAAS, 23, 991

Pearson, T. J., & Readhead, A. C. S. 1988, ApJ, 328, 114

Penston, M. V., & Fosbury, R. A. E. 1978, MNRAS, 183, 479

Perley, R. A. 1982, AJ, 87, 859

Readhead, A. C. S., Hough, D. H., Ewing, M. S., Walker, R. C., & Romney, J. D. 1983, ApJ, 265, 107

Readhead, A. C. S., Pearson, T. J., & Unwin, S. C. 1984, in IAU Symp. 110, VLBI and Compact Radio Sources, ed. R. Fanti, K. Kellerman, & G. Setti (Dordrecht: Reidel), 131

Readhead, A. C. S., & Wilkinson, P. N. 1978, ApJ, 223, 25

Rickett, B., & Coles, W. 1988, in IAU Symp. 129, The Impact of VLBI on Astrophysics and Geophysics, ed. M. J. Reid & J. M. Moran (Dordrecht: Kluwer), 287

Romani, R., Narayan, R., & Blandford, R. 1986, MNRAS, 220, 19

Rudnick, L., & Jones, T. W. 1982, ApJ, 255, 39

———. 1983, AJ, 88, 518

Scott, M. A., & Readhead, A. C. S. 1977, MNRAS, 180, 539

Seielstad, G. A., Pearson, T. J., & Readhead, A. C. S. 1983, PASP, 95, 842

Simard-Normandin, M., & Kronberg, P. P. 1980, ApJ, 242, 74

Spangler, S. R., & Gwinn, C. R. 1990, ApJ, 353, L29

Spencer, R. E., McDowell, J. C., Charlesworth, M., Fanti, C., Parma, P., & Peacock, J. A. 1989, MNRAS, 240, 657

Steppe, H., Salter, C. J., & Saikia, D. J. 1990, in Compact Steep Spectrum and GHz-Peaked Spectrum Radio Sources, ed. C. Fanti, R. Fanti, C. P. O'Dea, & R. T. Schilizzi (Bologna: Consiglio Nazionale delle Ricerche, Istituto di Radioastronomia), 44

van der Laan, H. 1966, Nature, 211, 1131

Waltman, E. B., Fiedler, R. L., Johnston, K. J., Spencer, J. H., Florkowski, D. R., Josties, F. J., McCarthy, D. D., & Matsakis, D. N. 1991, ApJS, 77, 379

Webber, J. C., DeNoyer, L. K., & Yang, K. S. 1975, BAAS, 7, 262

Webber, J. C., DeNoyer, L. K., Yang, K. S., & Swenson, G. W. 1976, AJ, 81, 1069

Webber, J. C., Yang, K. S., & Swenson, G. W. 1980, AJ, 85, 1434

Wills, B. J., Kraus, J. D., & Andrew, B. H. 1971, ApJ, 169, L87

Witzel, A., Pauliny-Toth, I. I. K., Geldzahler, B. J., & Kellermann, K. I. 1978, AJ, 83, 475

Witzel, A., Schmidt, J., Pauliny-Toth, I. I. K., & Nauber, U. 1979, 84, 942

Witzel, A., Veron, P., & Veron, M. P. 1971, A&A, 11, 171